

Learning to Advect: A Neural Semi-Lagrangian Architecture for Weather Forecasting

Carlos A. Pereira ^{*1} Stéphane Gaudreault ^{*1} Valentin Dallerit ¹ Christopher Subich ¹ Shoyon Panday ¹
 Siqi Wei ¹ Sasa Zhang ¹ Siddharth Rout ² Eldad Haber ² Raymond J. Spiteri ³ David Millard ⁴
 Emilia Diaconescu ¹

Abstract

Recent machine-learning approaches to weather forecasting often employ a monolithic architecture, where distinct physical mechanisms—advection (transport), diffusion-like mixing, thermodynamic processes, and forcing—are represented implicitly within a single large network. This representation is particularly problematic for advection, where long-range transport must be treated with expensive global interaction mechanisms or through deep, stacked convolutional layers. To mitigate this, we present PARADIS, a physics-inspired global weather prediction model that imposes inductive biases on network behavior through a functional decomposition into advection, diffusion, and reaction blocks acting on latent variables. We implement advection through a Neural Semi-Lagrangian operator that performs trajectory-based transport via differentiable interpolation on the sphere, enabling end-to-end learning of both the latent modes to be transported and their characteristic trajectories. Diffusion-like processes are modeled through depthwise-separable spatial mixing, while local source terms and vertical interactions are modeled via pointwise channel interactions, enabling operator-level physical structure. PARADIS provides state-of-the-art forecast skill at a fraction of the training cost. On ERA5-based benchmarks, the 1° PARADIS model—with a total training cost of less than a GPU-month—meets or exceeds the perfor-

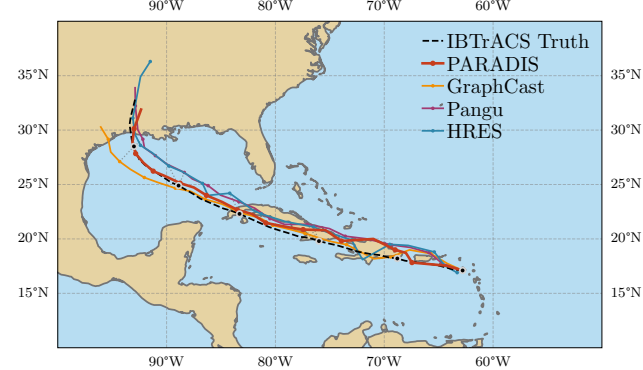


Figure 1. Tracking of cyclone eye for Hurricane Laura (August 2020) using different models and the observed trajectory (IBTrACS dataset (Knapp et al., 2010; Gahtan et al., 2024)).

mance of 0.25° traditional and machine-learning baselines, including the ECMWF HRES forecast and DeepMind’s GraphCast.

1. Introduction

Weather forecasting constitutes critical infrastructure for global safety and economic resilience, informing daily decisions and mitigating the impacts of extreme events. For decades, numerical PDE solvers have addressed this challenge. More recently, weather forecasting using machine learning has seen rapid progress.

The success of machine learning models has sparked important debate in the numerical weather prediction (NWP) community around fundamental questions: How can they forecast unprecedented extreme events? Can systems trained on only 40 years of historical data reliably predict climate extremes that have never been observed before (Ben-Bouallegue et al., 2025)? Although imperfect, these models have shown surprising robustness. For example, results reported so far indicate that they can successfully predict tropical cyclone trajectories (Bi et al., 2023; Lam et al., 2023), although significant challenges remain in forecasting cyclone intensity (Shi et al., 2025).

^{*}Equal contribution ¹Recherche en prévision numérique atmosphérique, Environnement et Changement climatique Canada, Dorval, Québec, Canada ²Department of Earth, Ocean and Atmospheric Sciences, University of British Columbia, Vancouver, British Columbia, Canada ³Department of Computer Science, University of Saskatchewan, Saskatoon, Saskatchewan, Canada ⁴Department of Mechanical Engineering, Rochester Institute of Technology, Rochester, USA. Correspondence to: Stéphane Gaudreault <stephane.gaudreault@ec.gc.ca>.

These observational shortcomings highlight a deeper structural issue: purely deep learning weather models lack the geometric constraints required for fine-scale fluid dynamics. Standard architectures, such as convolutions, message-passing, and attention, propagate information through local mixing, forcing long-range advection to emerge implicitly from deep stacks of operations that introduce diffusive artifacts (Zakariaei et al., 2024). Consequently, these models act as low-pass filters, washing out high-frequency details and making it difficult to relocate sharp features without smearing (Xu et al., 2024; Price et al., 2025). This smoothing is further compounded by mean-squared error (MSE) minimization, which induces a “double penalty” effect (Subich et al., 2025), driving models to predict a conditional mean rather than the realistic localized extremes required for high-stakes emergency planning.

We address this limitation by embedding a semi-Lagrangian transport algorithm directly into the neural architecture, introducing PARADIS (**P**hysically-inspired **A**dvection, **R**eaction And **D**iffusion on the **S**phere). Unlike classical semi-Lagrangian methods that advect known physical variables along solved velocity fields (Robert, 1981), PARADIS learns *which* latent features to transport and along *which* trajectories. By separating what to learn (transport modes) from how to represent it (Lagrangian trajectories), the model avoids expending representational capacity on re-learning atmospheric transport processes for which efficient algorithms already exist. This contrasts with convolution- or attention-based approaches, which offer limited explicit physical consistency.

We present a global PARADIS model at 1° resolution that achieves state-of-the-art forecasting performance via:

- **Neural semi-Lagrangian architecture:** We propose a neural operator that advects a compressed latent representation along flow trajectories on the sphere. This compression reduces the computational cost of advection and encourages the network to distinguish between atmospheric features that require transport and those processed locally.
- **Physics-inspired decomposition:** We enforce hard architectural constraints by decomposing the forecast operator into trajectory-based transport (advection), depthwise-separable spatial mixing (diffusion), and pointwise transformations (reaction). This discourages unphysical shortcuts and aligns network components with physical processes.
- **Spectral training curriculum:** We introduce a multi-stage curriculum that begins with a reversed Huber loss and concludes with spectral fine-tuning. This explicitly optimizes amplitude and phase, mitigating spectral roll-off and preserving small-scale energy.

2. Related Work

2.1. Data-Driven Weather Prediction Models

The emergence of data-driven models has transformed weather forecasting, arguably the most significant shift since Richardson’s pioneering work (Richardson, 1922). Enabled by comprehensive reanalysis datasets such as ERA5 (Hersbach et al., 2020), which translate raw meteorological observations into a model-space “truth” estimate and by rapid advances in deep learning, these models now rival operational NWP systems in deterministic skill. Vision Transformer-based models, including Pangu-Weather (Bi et al., 2023), FengWu (Chen et al., 2024), and FuXi (Chen et al., 2023), leverage self-attention to model long-range atmospheric dependencies, while Graph Neural Network (GNN) approaches such as GraphCast (Lam et al., 2023), the Artificial Intelligence Forecasting System (AIFS) (Lang et al., 2024a), and the work of Keisler (Keisler, 2022) represent the atmosphere on multiresolution meshes, enabling flexible treatment of spherical geometry beyond uniform latitude-longitude grids. In parallel, Fourier Neural Operators (FNO) (Bonev et al., 2023) seek to learn resolution-robust operator mappings of the underlying partial differential equations. Recent work addresses uncertainty and generalization limitations of deterministic surrogates, with diffusion-based generative models (Price et al., 2025; Li et al., 2023) targeting probabilistic forecasts of extreme events, large-scale foundation models such as Aurora (Bodnár et al., 2024) and Prithvi WxC (Schmude et al., 2024) exploring cross-resolution and multi-variable generalization through fine-tuning, and hybrid systems like NeuralGCM (Kochkov et al., 2024) integrating differentiable dynamical cores with learned physical parameterizations.

2.2. Advection–Diffusion–Reaction Network

Most directly relevant to our work is the Advection–Diffusion–Reaction Network (ADRNet) proposed by (Zakariaei et al., 2024). They demonstrated that standard convolutional neural networks are fundamentally limited in representing advection-dominated dynamics and introduced an architectural decomposition that improved performance compared with standard convolutional architectures.

However, this approach cannot be directly applied to global atmospheric forecasting. ADRNet was designed on regular two-dimensional Cartesian grids, failing to account for spherical geometry, multi-level states, and the need for spectral fidelity over long autoregressive rollouts, and the computational constraints imposed by training on large-scale reanalysis datasets. Addressing these challenges requires additional architectural innovations beyond a direct extension of existing ADR-style models.

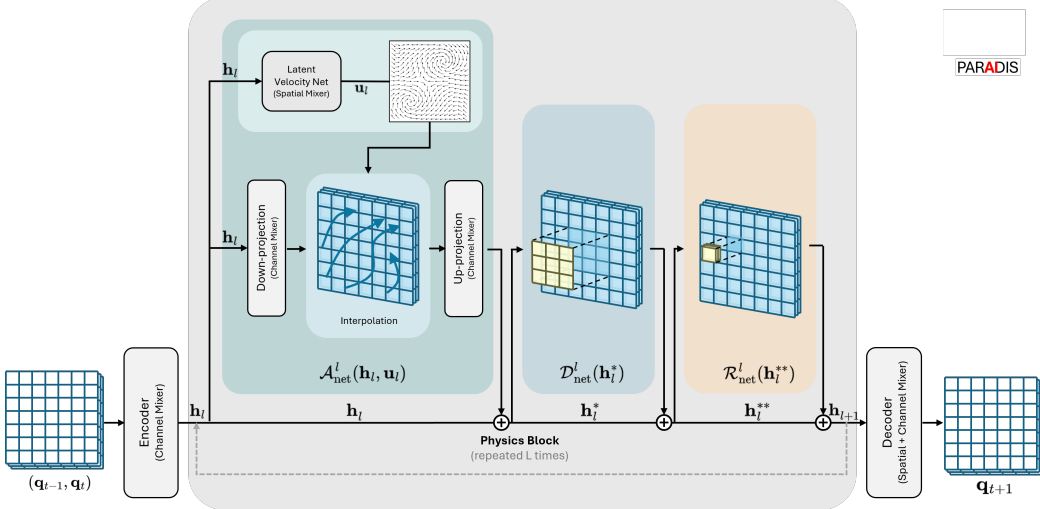


Figure 2. Diagram of the PARADIS model.

3. From Physical Principles to a Neural Architecture

Most neural weather models treat forecasting as an image-to-image translation task, learning patterns from data without explicit physical structure. This perspective neglects the fact that atmospheric dynamics are governed by conservation laws, where information is physically transported by fluid motion rather than transformed in place.

PARADIS is designed to mirror the Advection-Diffusion-Reaction structure that describes atmospheric evolution. At the coarsest level, the evolution of the state vector $\mathbf{q} \in \mathbb{R}^{C_{\text{phys}}}$ can be written as

$$\frac{\partial \mathbf{q}}{\partial t} + \underbrace{(\mathbf{u} \cdot \nabla) \mathbf{q}}_{\text{Advection}} = \underbrace{\mathcal{D}(\mathbf{q})}_{\text{Diffusion}} + \underbrace{\mathcal{R}(\mathbf{q})}_{\text{Reaction}}, \quad (1)$$

where \mathbf{u} is the velocity field. This decomposition naturally separates three physical processes: *Advection* (transport by wind), *Diffusion* (spatial mixing and dissipation), and *Reaction* (local transformations such as phase changes or radiative heating).

Rather than learning this structure from data, PARADIS enforces it architecturally: the network is explicitly decomposed into operators for advection, diffusion, and reaction as illustrated in Figure 2. In the following sections, we describe the main components of the model architecture.

3.1. Neural Semi-Lagrangian Architecture

3.1.1. MOTIVATING EXAMPLE: WHY EXPLICIT ADVECTION MATTERS

Advection is the dominant process in atmospheric dynamics: the transport of weather systems across the globe. Standard

CNNs struggle with this because convolution is a local operation with a fixed receptive field, so moving a feature across large distances requires a deep network with a larger parameter count, leading to a diffusive bias and inefficient or unstable learning dynamics.

To demonstrate the limitations of standard convolutions, we compare a 3-layer U-Net (Ronneberger et al., 2015) with our Neural Semi-Lagrangian (NSL) layer on a pure advection task (Figure 3). While the U-Net fails to represent the Gaussian tracer beyond its receptive field, the NSL layer, with only 20 learnable parameters, accurately relocates the feature. This suggests that explicit capture of long-range transport is a parameter-efficient way to include these dynamics, allowing devotion of a larger fraction of model capacity to inherently local nonlinear and forcing processes. See Section H for more details on this experiment.

3.1.2. ADVECTION VIA THE NEURAL SEMI-LAGRANGIAN OPERATOR

An NSL layer explicitly transports information along flow trajectories. A velocity network \mathcal{V}_{net} , implemented as a depthwise-separable convolution (Howard et al., 2017), estimates a set of transport fields from the latent state. These fields are learned from data to approximate the effective characteristics (curves) along which information propagates in the physical system. The model also learns which latent features are advected by which velocity fields.

The physical intuition behind this layer is that in a hyperbolic system of PDEs, such as those that approximate atmospheric motion, information is conserved along characteristic flow trajectories. To find the physical values at \mathbf{x} at time $t + \Delta t$, we ask: what information will arrive at \mathbf{x} ? We answer this by tracing backward in time to the parcel's

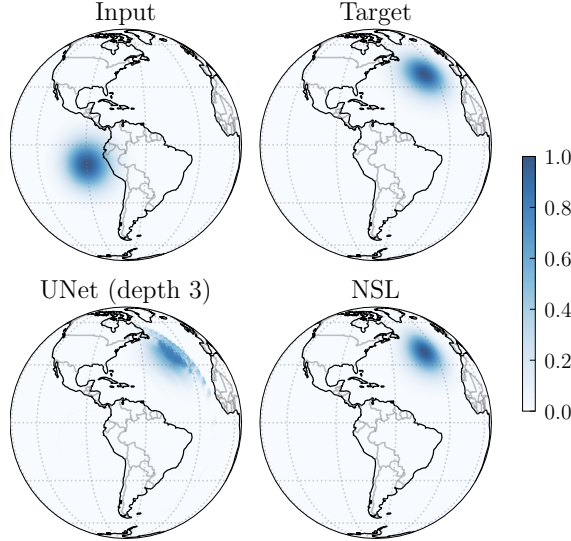


Figure 3. Comparison of implicit vs. explicit advection. An idealized experiment on a 721×1440 grid. *Top left*: Initial Gaussian tracer. *Top right*: Target state after advection under a spatially uniform wind. *Bottom left*: Prediction from a UNet of recursive depth 3, with about 44,000 total parameters. The fixed domain of dependence acts as a hard limit on how far information can be transported. *Bottom right*: Prediction from the Neural Semi-Lagrangian (NSL) layer with only 20 learnable parameters, which accurately relocates the tracer while preserving its structural integrity.

location at time t . For each grid point \mathbf{x} , we compute its departure point

$$\mathbf{x}_d = \mathbf{x} - \Delta t \cdot \mathbf{u}(\mathbf{x}). \quad (2)$$

Then, the new value of a set of features \mathbf{h} at \mathbf{x} is simply the old value at \mathbf{x}_d , i.e. $\mathbf{h}(\mathbf{x}, t + \Delta t) = \mathbf{h}(\mathbf{x}_d, t)$, which acts as a temporal increment.

By adopting this backward trajectory formulation, the layer retains the favorable stability properties of classical semi-Lagrangian schemes (Fletcher, 2019). The method is not restricted by the Courant–Friedrichs–Lowy (CFL) condition, meaning the time step is not limited by the grid spacing. Instead, the primary restriction arises from trajectory calculation convergence, governed by a Lipschitz condition on the velocity field that limits Δt in regions with large velocity gradients. As shown by (Smolarkiewicz & Pudykiewicz, 1992), this condition follows from the requirement that neighboring characteristics do not intersect, ensuring the uniqueness of the solution and the physical realizability of the flow (Cossette et al., 2014). The stability of the method can be extended to larger time steps through the composition of multiple Advection-Diffusion-Reaction layers, which act as a sub-stepping scheme.

To avoid singularities at the poles, we compute the departure location in a local rotated coordinate system centered at each

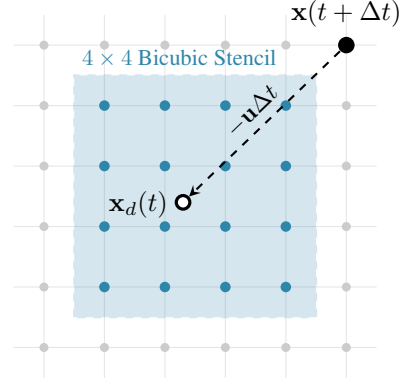


Figure 4. NSL Advection scheme. The value at the arrival grid point \mathbf{x} (●) is determined by tracing the trajectory backward to the off-grid departure point \mathbf{x}_d (○). The value at \mathbf{x}_d is then computed via interpolation using the surrounding stencil of active grid points.

grid point (McDonald & Bates, 1989). This approach treats each trajectory calculation in its own local frame, where standard planar geometry applies. The rotated coordinates are then transformed back to standard latitude-longitude via spherical trigonometry (see Section J.1 for details).

Because the computed departure point \mathbf{x}_d generally falls between grid points, we sample the feature map at this location using bicubic interpolation as illustrated in Figure 4. We choose bicubic over bilinear interpolation to minimize unwanted diffusion during the advection step. This operation is fully differentiable, allowing gradients to flow back into the velocity estimator. Additionally, the network’s overall computational cost is linear in the number of grid elements, N_{grid} , significantly cheaper than the $O(N_{\text{grid}}^2)$ cost of attention.

We implement this operation on a latent set of features $\mathbf{h} \in \mathbb{R}^{C_{\text{lat}}}$, which has a large number of channels $C_{\text{lat}} \gg C_{\text{phys}}$. Advection the full latent state can become computationally expensive. We posit that atmospheric waves compress into a smaller set of “transportable modes” that move coherently. Unlike classical semi-Lagrangian schemes, PARADIS learns both which features to transport and their characteristic velocity fields.

We therefore project \mathbf{h} down to a subspace C_{adv} using pointwise convolutions, with $C_{\text{phys}} < C_{\text{adv}} < C_{\text{lat}}$, apply the advection operator, and subsequently project back to the full latent space. This forces the network to discover a compressed representation of advected quantities, analogous to identifying the characteristic curves of the governing PDEs. The model learns end-to-end which combinations of atmospheric state are best represented through coherent spatial transport versus local transformation.

3.2. Physics-Inspired Decomposition

In PARADIS, we solve the conservation law (1) in a latent space. In this sense, we outline what a latent-space formulation of physical dynamics looks like. This includes an encoder–processor–decoder methodology. In the following sections, we describe the physical intuition behind this approach and how the physical decomposition allows this method to be separated into a latent evolution of features, a latent diffusion, and a latent reaction term. More details on the implementation are provided in Section B.

3.2.1. LATENT FEATURE REPRESENTATION

Atmospheric flows exist as the composition of larger structures that locally combine to produce observed weather. Large, synoptic-scale flows (scales larger than 1000km) in the atmosphere are governed by Rossby waves (planetary-scale, rotation-driven waves) that balance pressure gradients against the Earth’s rotation, small-scale flows are more strongly governed by gravity waves (buoyancy-driven waves), and moisture is passively advected until condensation or evaporation releases or absorbs latent heat. Each kind of motion is governed by its own set of wave speeds. Although we do not specify this decomposition a priori, we project the physical features to a rich-enough space, expecting that the encoder can differentiate these modes.

The physical variables of the atmosphere are mapped to a latent representation $\mathbf{h}(\mathbf{x}, t) \in \mathbb{R}^{C \times H \times W}$. Here, C denotes the latent channel capacity, while H and W represent the spatial grid dimensions. The mapping is performed by a linear encoder using a pointwise convolution (Section B.4.1). This acts as a vertical mixer, expanding C_{in} inputs to C_{lat} channels without altering the spatial structure. On output, we decode to C_{out} channels using a two-stage linear operator (Section B.4.2) consisting of a spatial mixer and a final channel-wise projection.

Working in this latent space, we reformulate Eq. (1) in Lagrangian form. The material derivative $D/Dt \equiv \partial/\partial t + \mathbf{u} \cdot \nabla$ describes the rate of change following fluid parcels, naturally separating advective transport from local forcings. In a continuous-time limit, the full system becomes

$$\mathbf{h}(\mathbf{x}, t) = \mathcal{E}(\mathbf{q}(\mathbf{x}, t)), \quad (3)$$

$$\frac{d\mathbf{x}}{dt} = \mathcal{V}_{\text{net}}, \quad (4)$$

$$\frac{D\mathbf{h}}{Dt} = \mathcal{D}_{\text{net}}(\mathbf{h}) + \mathcal{R}_{\text{net}}(\mathbf{h}), \quad (5)$$

$$\mathbf{q}(\mathbf{x}, t) = \mathcal{G}(\mathbf{h}(\mathbf{x}, t)), \quad (6)$$

where \mathcal{E} and \mathcal{G} are respectively the encoder and decoder, \mathcal{V}_{net} represents learned transport velocities, and \mathcal{D}_{net} and \mathcal{R}_{net} are neural residual operators for diffusion and reaction, respectively. Inside the material derivative, \mathcal{A}_{net} acts as the residual update for the advection operation.

To evolve the latent state from t to $t + \Delta t$, N_{sub} sub-steps are taken. At each sub-step l , to evolve from \mathbf{h}_l to \mathbf{h}_{l+1} , we employ the well-known Lie–Trotter operator-splitting method to integrate each physical process sequentially:

$$\mathbf{u}_l = \mathcal{V}_{\text{net}}^l(\mathbf{h}_l), \quad (7)$$

$$\mathbf{h}_l^* = \mathbf{h}_l + \mathcal{A}_{\text{net}}^l(\mathbf{h}_l, \mathbf{u}_l), \quad (8)$$

$$\mathbf{h}_l^{**} = \mathbf{h}_l^* + \mathcal{D}_{\text{net}}^l(\mathbf{h}_l^*), \quad (9)$$

$$\mathbf{h}_{l+1} = \mathbf{h}_l^{**} + \mathcal{R}_{\text{net}}^l(\mathbf{h}_l^{**}). \quad (10)$$

Here, $\mathcal{V}_{\text{net}}^l$ predicts effective transport flows from the current state, and (8)–(10) are structured as residual operators, which facilitate learning. By stacking these split operators, the network learns to integrate the governing equations end-to-end while maintaining architectural constraints at the operator level.

Once the variables are projected into the latent space, the network performs an advection step as described in Section 3.1.2. The specific hyperparameters used in this work are described in the appendix (Table 2).

3.2.2. DIFFUSION (SPATIAL MIXING)

The diffusion term $\mathcal{D}_{\text{net}}(\mathbf{h})$ represents sub-grid mixing and dissipation. In numerical methods, this is often modeled via Laplacian-like stencils. We implement this using depthwise separable convolutions with a 3×3 kernel. The depthwise component applies a learned spatial stencil to each channel, similar to a finite-difference Laplacian. A subsequent pointwise projection (1×1 convolution) mixes channels to model anisotropic or cross-variable diffusion.

To efficiently capture large-scale static forcings (e.g., topographic effects) without the parameter cost of full-resolution bias tensors, we augment these operators with a *Low-Rank Bias* mechanism (see Section B.1.3). By decomposing the bias field into rank- K spatial factors, this approach allows the model to learn spatially coherent global corrections while maintaining a minimal memory footprint.

3.2.3. REACTION (POINTWISE MIXING)

The reaction term $\mathcal{R}_{\text{net}}(\mathbf{h})$ represents local thermodynamic and microphysical processes where variables interact at a fixed location. We implement this using two consecutive pointwise (1×1) convolutions with an intermediate Swish (Hendrycks, 2016) activation function for nonlinearity. Here, we mix information across channels without spatial propagation, strictly adhering to the locality of the reaction operator. Since the vertical levels of the atmosphere are stacked within the channel dimension, vertical dynamics and column-wise coupling are effectively handled by this reaction mechanism.

3.2.4. SPHERICAL GEOMETRY AND BOUNDARY CONDITIONS

Global weather models face a geometric challenge: the Earth’s latitude-longitude grid has singularities at the poles. We address this with Geocyclic Padding (Cheon et al., 2024).

Along the longitude direction, we use periodic boundaries: data at the last longitude degree connects directly to longitude 0° . At the poles, where all meridians converge, we apply “rolled” padding: information crossing the North Pole emerges on the opposite side, rotated 180° in longitude. This preserves physical continuity as air parcels cross polar regions.

Additionally, we enforce scalar continuity at the multiple grid points located at the poles by averaging features over all such points along each channel, preventing accumulation of grid-scale noise at the convergence points.

3.3. Training Curriculum for Spectral Preservation

To mitigate the “double penalty” effect (Subich et al., 2025) of the standard mean squared error training, PARADIS adopts a three-phase curriculum that incorporates a custom loss function with spectral refinement.

3.3.1. REVERSED HUBER LOSS

Phase 1 employs a reversed Huber loss defined in eq. (11). For prediction error $e = y - \hat{y}$ and threshold δ , the loss is:

$$L_\delta(e) = \begin{cases} \delta|e|, & |e| \leq \delta, \\ \frac{1}{2}e^2 + \frac{1}{2}\delta^2, & |e| > \delta. \end{cases} \quad (11)$$

Unlike standard Huber loss, which is quadratic for small errors and linear for large ones, this formulation penalizes small errors linearly and larger errors quadratically. This design reflects the priorities of weather forecasting: avoiding catastrophic forecast failures by strongly penalizing large errors through quadratic growth, while maintaining a more tolerant linear penalty for small errors.

3.3.2. AUTOREGRESSIVE FINE-TUNING

Phase 2 extends the model to multi-step forecasting through autoregressive rollouts. We gradually increase the forecast horizon from 12h to 72h in six stages, accumulating losses across all predicted lead times and backpropagating through the full trajectory. This mitigates exposure bias and enforces dynamical consistency under repeated application.

3.3.3. SPECTRAL FINE-TUNING

Phase 3 addresses the double penalty effect directly by fine-tuning in the spherical harmonic domain using an adjusted mean square error (AMSE) loss (Subich et al., 2025).

This loss separately penalizes amplitude and phase errors when modes are grouped by total wavenumber, allowing the model to maintain realistic small-scale energy even when precise positioning becomes unpredictable at longer lead times. We employ a progressive curriculum with increasing rollout horizons (1, 2, 4, 8, 12 steps), improving multiscale energy representation without expensive generative training.

Full details of each of these training phases, including the learning rate and number of steps used, are described in Section C.4.

4. Numerical Experiments

In this section, we evaluate the predictive performance and physical consistency of the PARADIS architecture. We benchmark our forecasts against ECMWF IFS HRES, DeepMind’s GraphCast, and Huawei’s Pangu Weather, using ERA5 reanalysis as the ground truth. Our evaluation focuses on three primary dimensions: lead-time forecast skill, error distribution across vertical profiles, and multiscale spectral fidelity. We provide analysis for standard meteorological variables, including geopotential ¹ (z), temperature (t), wind components (u, v), and surface fields such as 2-metre temperature ($2t$) and mean sea-level pressure (msl).

Computational cost. Training of PARADIS was performed on a distributed cluster of 32 NVIDIA H100 GPUs for approximately 0.8 GPU-months. Once trained, the model produces a 10-day 1° forecast in 3.5 GPU-seconds.

Evaluation setup. PARADIS is trained on ERA5 reanalysis data subsampled to 1° , spanning 1990–2019 and evaluated on the year 2020. This evaluation period is chosen to ensure a consistent comparison across all baseline datasets as curated in the WeatherBench 2 framework. We note that we have also performed these evaluations at later years, confirming consistency in the results shown here. All models are evaluated in fully autoregressive inference mode. Forecasts are initialized every 36 hours over the verification period, yielding independent forecast trajectories for each lead time. Verification metrics are computed by averaging errors across all initialization times and grid points at each forecast horizon.

Resolution, fairness, and scale-aware evaluation. PARADIS is trained and evaluated at 1° , using ERA5 fields downsampled to the same 1° grid as verification, ensuring consistent information content between training targets and

¹Geopotential is the gravitational potential energy corresponding to a given pressure level, given by multiplying the height above sea level by the acceleration due to gravity. The geopotential at the 500hPa level represents the “middle” of the atmosphere, and its topology acts as the steering flow for surface weather systems.

Table 1. RMSE for selected atmospheric variables at multiple pressure levels and 1, 5, and 10-day lead times. Bold indicates the best-performing model and underlining indicates the second-best.

Model	z_{500}			t_{850}			q_{700}		
	1d	5d	10d	1d	5d	10d	1d	5d	10d
HRES	4.38e+01	3.09e+02	8.00e+02	7.37e-01	1.93e+00	3.70e+00	7.71e-04	1.47e-03	1.97e-03
GraphCast	4.05e+01	<u>2.78e+02</u>	<u>7.29e+02</u>	5.66e-01	<u>1.61e+00</u>	<u>3.38e+00</u>	5.19e-04	1.11e-03	1.64e-03
Pangu	4.76e+01	2.99e+02	7.84e+02	6.78e-01	1.76e+00	3.59e+00	5.97e-04	1.26e-03	1.85e-03
PARADIS	3.94e+01	2.73e+02	7.27e+02	<u>5.79e-01</u>	1.59e+00	3.33e+00	<u>5.31e-04</u>	<u>1.15e-03</u>	<u>1.72e-03</u>
PARADIS AMSE	<u>4.01e+01</u>	2.91e+02	7.87e+02	6.03e-01	1.68e+00	3.50e+00	5.42e-04	<u>1.23e-03</u>	<u>1.81e-03</u>
Model	u_{850}			v_{850}			w_{850}		
	1d	5d	10d	1d	5d	10d	1d	5d	10d
HRES	1.52e+00	3.99e+00	6.68e+00	1.52e+00	3.98e+00	6.71e+00	2.62e-01	3.26e-01	3.58e-01
GraphCast	<u>1.10e+00</u>	<u>3.25e+00</u>	5.87e+00	<u>1.10e+00</u>	<u>3.27e+00</u>	5.88e+00	1.25e-01	<u>1.66e-01</u>	<u>1.95e-01</u>
Pangu	1.29e+00	3.52e+00	6.32e+00	1.30e+00	3.56e+00	6.33e+00	-	-	-
PARADIS	1.09e+00	3.20e+00	<u>5.87e+00</u>	1.10e+00	3.22e+00	<u>5.90e+00</u>	1.04e-01	1.50e-01	1.81e-01
PARADIS AMSE	1.11e+00	3.42e+00	6.33e+00	1.12e+00	3.46e+00	6.36e+00	<u>1.09e-01</u>	1.71e-01	2.14e-01

evaluation space. Baseline forecasts are evaluated on this identical 1° grid using the same coarsening approach, enabling a like-for-like comparison at that resolution. To avoid conflating nominal grid spacing with physical skill, we additionally report spectral metrics in the spherical harmonic space. Mode-by-mode spectral coherence directly measures phase fidelity by total wavenumber and is independent of the native output grid (Figure 15 in Appendix). Experiments in which 1° PARADIS forecasts are interpolated to 0.25° are also shown in the appendix; since interpolation cannot introduce new small-scale information, these tests favor native 0.25° models, yet the conclusions at moderate lead times remain unchanged. See Section F.5 for a more detailed discussion of this effect.

4.1. Lead-Time Forecast Skill

Table 1 reports RMSE values for select variables, pressure levels, and lead times. Despite operating at a coarser 1° spatial resolution than the 0.25° baseline models, PARADIS achieves best or second-best performance across nearly all entries. Notably, improvements in dynamical variables like wind components (u, v) and vertical velocity (w) underscore the effectiveness of trajectory-based latent transport. The evolution of RMSE for these models across a broader range of lead times is provided in Section F and Figure 11.

4.2. Vertical Structure of Forecast Errors.

To assess how forecast skill varies with altitude, Figure 5 presents vertical RMSE differences between PARADIS and IFS HRES as a function of lead time. Negative values indicate lower error for PARADIS (represented in blue). Skill gains are most pronounced in altitudes near the surface, where more complex dynamics exist. These results indicate that the benefits of explicit latent-space transport are stronger for smaller-scale atmospheric dynamics, where coherent advection dominates error growth.

4.3. Multiscale and Spectral Fidelity

Deterministic neural forecasts are known to suffer from overly smooth fields at medium and small scales. Figure 6 (top) evaluates this effect for z_{500} at a 3-day lead time via a spectral decomposition. We observe that PARADIS exhibits equal or higher spectral fidelity by total wavenumber than GraphCast, particularly at intermediate and high wavenumbers. This is visible in the PARADIS (Phase 2) curve, which uses a similar training curriculum to GraphCast. PARADIS-AMSE (Phase 3) further improves small-scale energy retention via spectral finetuning. While this results in a slight degradation of RMSE compared to Phase 2 (see Figure 6, bottom), this behavior is consistent with the *perception-distortion trade-off* (Blau & Michaeli, 2018). This theoretical bound suggests that as a reconstruction becomes more spectrally faithful to the natural distribution (lower perceptual error), its pointwise distortion (e.g., RMSE) must necessarily increase. We argue this trade-off is desirable for physical consistency in weather forecasting, prioritizing the preservation of small-scale energy critical for capturing extreme events over minimizing smoothed error.

4.4. Cyclone Tracking

We further evaluate forecast skill on tropical cyclone intensity and track errors, which provide stringent tests of dynamical consistency and long-range transport. Although PARADIS operates at a coarser 1° resolution, it produces cyclone track forecasts that are comparable to, and in some lead times more accurate than, those of higher-resolution models, as illustrated for Hurricane Laura (August 2020) in Figure 1. A more robust analysis, including mean direct position errors across over 80 storms in the year 2020, is shown in Figure 7, where PARADIS yields lower or comparable error than GraphCast, Pangu, and HRES without access to high-resolution input data. PARADIS shows a similar intensity error (weakening) trend as the machine learning baselines, but its initial error is greater as hurricane

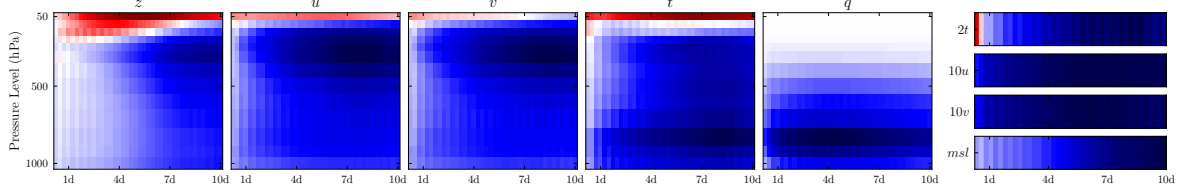


Figure 5. Vertical and surface RMSE differences between PARADIS and ECMWF HRES as a function of forecast lead time. Shown are area-weighted RMSE differences (PARADIS minus HRES) for atmospheric variables evaluated across pressure levels. Negative values (blue) indicate lower error for PARADIS relative to HRES. Results demonstrate increasing skill gains for PARADIS with lead time, particularly in the mid- to upper-troposphere and for dynamical variables.

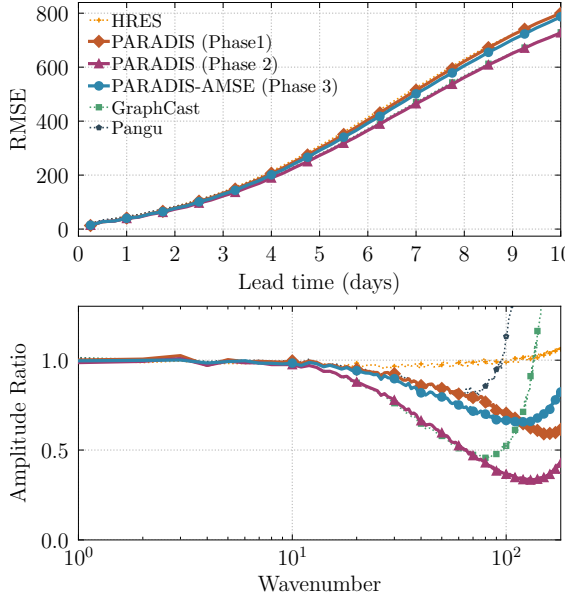


Figure 6. Comparison of RMSE (top, lower is better) and spectral amplitude ratio (bottom, per Section E.3; closer to 1 is better) of different phases in PARADIS and baseline models, for z_{500} variable with the spectra computed at the 3-day lead time.

cores are poorly-resolved on a 1° grid.

5. Conclusion

In this work, we introduced PARADIS, a neural weather forecasting architecture that draws inspiration from classical numerical methods by structurally decomposing a forecast operator into advection, diffusion, and reaction components. By embedding a differentiable semi-Lagrangian operator directly into the network, the model learns to transport latent atmospheric features along characteristic trajectories, effectively decoupling long-range motion from local processing.

Our experiments demonstrate that the PARADIS model produces physically meaningful forecast skill. Despite operating at a coarse 1° resolution, the model achieves best or second-best RMSE across most evaluated variables and lead times when compared to 0.25° baselines. Importantly, PARADIS also produces competitive tropical cyclone track

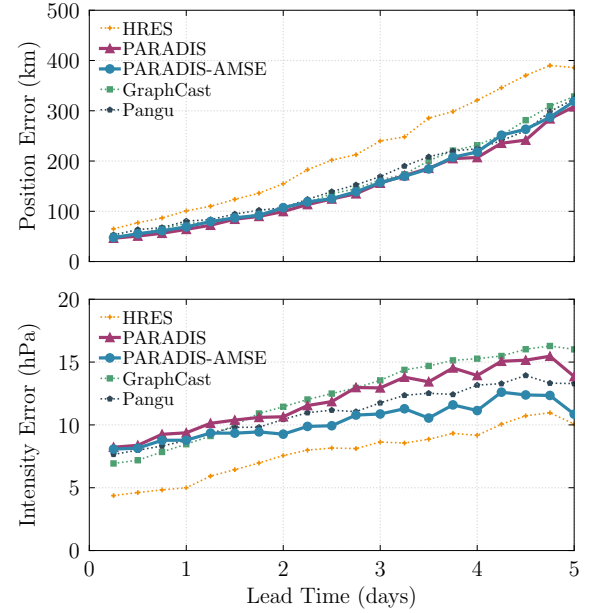


Figure 7. Position and intensity errors for PARADIS and other models relative to observed cyclone tracks over the 2020 evaluation period; lower values indicate better performance.

forecasts: across more than 80 storms in 2020, it matches or outperforms higher-resolution learned models in mean position error, highlighting the importance of accurate large-scale transport over fine-grid detail

Finally, we address the pervasive issue of spectral roll-off and the double-penalty effect through a three-stage training curriculum that combines the reversed Huber loss, autoregressive fine-tuning, and spectral optimization. This curriculum improves phase coherence and small-scale energy retention, yielding spectral fidelity that matches or exceeds strong baselines while maintaining competitive RMSE. Looking forward, we aim to scale PARADIS to higher resolutions, limited-area modeling, and probabilistic extensions. The performance and physical consistency of PARADIS suggest that integrating explicit physical operators with neural architectures represents a robust pathway for the design of the next generation of weather prediction systems.

Code Availability

The implementation of the PARADIS model presented in this work is available on GitHub at https://github.com/Wx-Alliance-Alliance-Meteo/paradis_model.

Acknowledgements

We would like to acknowledge the collaboration of our colleagues and the support of the managers of the *Direction de la recherche en météorologie* and the *Division du développement des prévisions nationales* at Environment and Climate Change Canada. We also gratefully acknowledge the valuable contributions of Ben Adcock, Mahta Abdollahzadehzare, Avi Gupta, Mehdi Haned, Erika Kember, Francis Poulin, Steven Ruuth, Aryan Sharma, Seth Taylor, and Xiangye Xu.

Impact Statement

This paper advances machine learning for weather forecasting, a domain with major life-safety and economic implications. We emphasize that weather prediction systems extend beyond individual forecasting algorithms, encompassing end-to-end workflows from data assimilation to post-processing and policy guidance. Accordingly, new methods should be adopted only after rigorous, system-level verification over time horizons sufficient to evaluate extreme events and out-of-distribution performance.

We acknowledge the carbon footprint associated with training large-scale models. However, the results in this work support the view that explicit transport enables a 1° model to match the effective resolution of substantially more expensive systems at medium lead times.

References

3. URL <https://www.nature.com/articles/s41586-023-06185-3>. Number: 7970 Publisher: Nature Publishing Group.
- Blau, Y. and Michaeli, T. The perception-distortion trade-off. In *Proceedings of the IEEE conference on computer vision and pattern recognition*, pp. 6228–6237, 2018.
- Bodnár, C., Behrmann, G., Li, S., Pratik, K., et al. Aurora: A foundation model of the atmosphere. *arXiv preprint arXiv:2405.13063*, 2024.
- Bonev, B., Kurth, T., Hundt, C., Pathak, J., Baust, M., Kashinath, K., and Anandkumar, A. Spherical fourier neural operators: Learning stable dynamics on the sphere. In *International Conference on Machine Learning*, pp. 2806–2823. PMLR, 2023.
- Chen, K., Han, T., Gong, J., Bai, L., Ling, F., Luo, J.-H., Chen, X., Ma, L., Zhang, T., Su, R., et al. Fengwu: Pushing the skill of global weather forecasts to 10 days. *Journal of Advances in Modeling Earth Systems*, 16(5):e2023MS003926, 2024.
- Chen, L., Zhong, X., Zhang, F., Cheng, Y., Xu, Y., Qi, Y., and Li, H. Fuxi: A cascade machine learning forecasting system for 15-day global weather forecast. *npj Climate and Atmospheric Science*, 6(1):190, 2023.
- Cheon, M., Choi, Y.-H., Kang, S.-Y., Choi, Y., Lee, J.-G., and Kang, D. Karina: An efficient deep learning model for global weather forecast. *arXiv preprint arXiv:2403.10555*, 2024.
- Cossette, J.-F., Smolarkiewicz, P. K., and Charbonneau, P. The Monge-Ampere trajectory correction for semi-Lagrangian schemes. *Journal of Computational Physics*, 274(1):208–229, 2014.
- Fletcher, S. J. *Semi-Lagrangian Advection Methods and Their Applications in Geoscience*. Elsevier, 2019.
- Gahtan, J., Knapp, K. R., Schreck, C. J., Diamond, H. J., Kossin, J. P., and Kruk, M. C. International best track archive for climate stewardship (IBTrACS) project, version 4r01, 2024. URL <https://doi.org/10.25921/82ty-9e16>.
- Hendrycks, D. Gaussian error linear units (gelus). *arXiv preprint arXiv:1606.08415*, 2016.
- Hersbach, H., Bell, B., Berrisford, P., Hirahara, S., Horányi, A., Muñoz-Sabater, J., Nicolas, J., Peubey, C., Radu, R., Schepers, D., et al. The ERA5 global reanalysis. *Quarterly Journal of the Royal Meteorological Society*, 146(730):1999–2049, 2020.

Howard, A. G., Zhu, M., Chen, B., Kalenichenko, D., Wang, W., Weyand, T., Andreetto, M., and Adam, H. Mobilenets: Efficient convolutional neural networks for mobile vision applications. *CoRR*, abs/1704.04861, 2017. URL <http://arxiv.org/abs/1704.04861>.

Hu, S., Tu, Y., Han, X., He, C., Cui, G., Long, X., Zheng, Z., Fang, Y., Huang, Y., Zhao, W., Zhang, X., Thai, Z. L., Zhang, K., Wang, C., Yao, Y., Zhao, C., Zhou, J., Cai, J., Zhai, Z., Ding, N., Jia, C., Zeng, G., Li, D., Liu, Z., and Sun, M. MiniCPM: Unveiling the Potential of Small Language Models with Scalable Training Strategies, June 2024. URL <http://arxiv.org/abs/2404.06395>. arXiv:2404.06395 [cs].

Huber, P. J. Robust estimation of a location parameter. In *Breakthroughs in Statistics: Methodology and Distribution*, pp. 492–518. Springer, 1992.

Keisler, R. Forecasting Global Weather with Graph Neural Networks, February 2022. URL <http://arxiv.org/abs/2202.07575>. arXiv:2202.07575 [physics].

Knapp, K. R., Kruk, M. C., Levinson, D. H., Diamond, H. J., and Neumann, C. J. The international best track archive for climate stewardship (ibtracs) unifying tropical cyclone data. *Bulletin of the American Meteorological Society*, 91(3):363–376, 2010.

Kochkov, D., Yuval, J., Langmore, I., Norgaard, P., Smith, J., Mooers, G., Klöwer, M., Lottes, J., Rasp, S., Düben, P., Hatfield, S., Battaglia, P., Sanchez-Gonzalez, A., Willson, M., Brenner, M. P., and Hoyer, S. Neural general circulation models for weather and climate. *Nature*, 632(8027):1060–1066, August 2024. ISSN 1476-4687. doi: 10.1038/s41586-024-07744-y. URL <https://www.nature.com/articles/s41586-024-07744-y>. Publisher: Nature Publishing Group.

Lam, R., Sanchez-Gonzalez, A., Willson, M., Wirnsberger, P., Fortunato, M., Alet, F., Ravuri, S., Ewalds, T., Eaton-Rosen, Z., Hu, W., et al. Learning skillful medium-range global weather forecasting. *Science*, 382(6677):1416–1421, 2023.

Lang, S., Alexe, M., Chantry, M., Dramsch, J., Pinault, F., Raoult, B., Clare, M. C., Lessig, C., Maier-Gerber, M., Magnusson, L., et al. AIFS–ECMWF’s data-driven forecasting system. *arXiv preprint arXiv:2406.01465*, 2024a.

Lang, S., Alexe, M., Clare, M. C. A., Roberts, C., Adewoyin, R., Bouallègue, Z. B., Chantry, M., Dramsch, J., Dueben, P. D., Hahner, S., Maciel, P., Prieto-Nemesio, A., O’Brien, C., Pinault, F., Polster, J., Raoult, B., Tietsche, S., and Leutbecher, M. AIFS-CRPS: Ensemble forecasting using a model trained with a loss function based on the Continuous Ranked Probability Score, December 2024b. URL <http://arxiv.org/abs/2412.15832>. arXiv:2412.15832 [physics].

Li, L., Carver, R., Lopez-Gomez, I., Sha, F., and Anderson, J. SEEDS: Emulation of Weather Forecast Ensembles with Diffusion Models, September 2023. URL <http://arxiv.org/abs/2306.14066>. arXiv:2306.14066 [physics].

Loshchilov, I. and Hutter, F. Decoupled weight decay regularization. *arXiv preprint arXiv:1711.05101*, 2017.

McDonald, A. and Bates, J. Semi-Lagrangian integration of a gridpoint shallow water model on the sphere. *Monthly Weather Review*, 117(1):130–137, 1989.

Murphy, A. H. and Epstein, E. S. Skill Scores and Correlation Coefficients in Model Verification. *Monthly Weather Review*, 117(3):572–582, March 1989. ISSN 1520-0493, 0027-0644. doi: 10.1175/1520-0493(1989)117<572:SSACCI>2.0.CO;2. URL https://journals.ametsoc.org/view/journals/mwre/117/3/1520-0493_1989_117_0572_ssacci_2_0_co_2.xml. Publisher: American Meteorological Society Section: Monthly Weather Review.

Price, I., Sanchez-Gonzalez, A., Alet, F., Andersson, T. R., El-Kadi, A., Masters, D., Ewalds, T., Stott, J., Mohamed, S., Battaglia, P., et al. Probabilistic weather forecasting with machine learning. *Nature*, 637(8044):84–90, 2025.

Rasp, S., Hoyer, S., Merose, A., Langmore, I., Battaglia, P., Russell, T., Sanchez-Gonzalez, A., Yang, V., Carver, R., Agrawal, S., Chantry, M., Ben Bouallègue, Z., Dueben, P., Bromberg, C., Sisk, J., Barrington, L., Bell, A., and Sha, F. WeatherBench 2: A Benchmark for the Next Generation of Data-Driven Global Weather Models. *Journal of Advances in Modeling Earth Systems*, 16(6):e2023MS004019, 2024a. ISSN 1942-2466. doi: 10.1029/2023MS004019. URL <https://onlinelibrary.wiley.com/doi/abs/10.1029/2023MS004019>.

Rasp, S., Hoyer, S., Merose, A., Langmore, I., Battaglia, P., Russell, T., Sanchez-Gonzalez, A., Yang, V., Carver, R., Agrawal, S., et al. Weatherbench 2: A benchmark for the next generation of data-driven global weather models. *Journal of Advances in Modeling Earth Systems*, 16(6):e2023MS004019, 2024b.

Richardson, L. F. *Weather prediction by numerical process*. Cambridge University Press, 1922.

Robert, A. A stable numerical integration scheme for the primitive meteorological equations. *Atmosphere-Ocean*, 19(1):35–46, 1981.

Ronneberger, O., Fischer, P., and Brox, T. U-Net: Convolutional Networks for Biomedical Image Segmentation. In Navab, N., Hornegger, J., Wells, W. M., and Frangi, A. F. (eds.), *Medical Image Computing and Computer-Assisted Intervention – MICCAI 2015*, pp. 234–241, Cham, 2015. Springer International Publishing. ISBN 978-3-319-24574-4. doi: 10.1007/978-3-319-24574-4_28.

Schmude, J., Roy, S., Trojak, W., Jakubik, J., Civitarese, D. S., Singh, S., Kuehnert, J., Ankur, K., Gupta, A., Phillips, C. E., Kienzler, R., Szwarcman, D., Gaur, V., Shinde, R., Lal, R., Da Silva, A., Diaz, J. L. G., Jones, A., Pfreundschuh, S., Lin, A., Sheshadri, A., Nair, U., Anantharaj, V., Hamann, H., Watson, C., Maskey, M., Lee, T. J., Moreno, J. B., and Ramachandran, R. Prithvi WxC: Foundation Model for Weather and Climate, September 2024. URL <http://arxiv.org/abs/2409.13598>. arXiv:2409.13598 [physics].

Shi, X., Chen, G., Zhang, Q., et al. Comparison of ai and nwp models in operational severe weather forecasting: A study on tropical cyclone predictions. *Journal of Geophysical Research: Machine Learning and Computation*, 2(1):e2024JH000123, 2025.

Smolarkiewicz, P. K. and Pudykiewicz, J. A. A class of semi-Lagrangian approximations for fluids. *Journal of the Atmospheric Sciences*, 49(22):2082–2096, 1992.

Subich, C., Husain, S. Z., Separovic, L., and Yang, J. Fixing the Double Penalty in Data-Driven Weather Forecasting Through a Modified Spherical Harmonic Loss Function. In Singh, A., Fazel, M., Hsu, D., Lacoste-Julien, S., Berkenkamp, F., Maharaj, T., Wagstaff, K., and Zhu, J. (eds.), *Proceedings of the 42nd International Conference on Machine Learning*, volume 267 of *Proceedings of Machine Learning Research*, Vancouver, Canada, July 2025. PMLR. URL <https://raw.githubusercontent.com/mlresearch/v267/main/assets/subich25a/subich25a.pdf>.

Wald, L. Basics in solar radiation at Earth surface v2, July 2019. URL <https://hal.science/hal-02175988>. Working paper.

Xu, W., Chen, K., Han, T., Chen, H., Ouyang, W., and Bai, L. Extremecast: Boosting extreme value prediction for global weather forecast. *arXiv preprint arXiv:2402.01295*, 2024.

Zakariaei, N., Rout, S., Haber, E., and Eliasof, M. Advection augmented convolutional neural networks. *arXiv preprint arXiv:2406.19253*, 2024.

A. The PARADIS Model

The PARADIS (*Physically-inspired Advection, Reaction And Diffusion on the Sphere*) architecture is grounded in the perspective of flow evolution in fluid dynamics. Rather than treating the evolution of the atmospheric state as a black-box sequence of transformations, we formulate it as latent-space dynamics governed by an explicit advection–diffusion–reaction system.

In the continuous-time limit, the evolution of the latent state \mathbf{h} at a spatial location \mathbf{x} is governed by the material derivative $\frac{D}{Dt}$, which describes the rate of change following a fluid parcel

$$\frac{D\mathbf{h}}{Dt} = \frac{\partial \mathbf{h}}{\partial t} + (\mathbf{u} \cdot \nabla) \mathbf{h} = \mathcal{D}(\mathbf{h}) + \mathcal{R}(\mathbf{h}), \quad (12)$$

where \mathbf{u} is a velocity field that satisfies

$$\frac{d\mathbf{x}}{dt} = \mathbf{u}, \quad (13)$$

This formulation naturally separates the *conservative transport* (advection) from the *local physical processes* (diffusion and reaction). The processor in PARADIS acts as a neural numerical integrator for this system. A reference for symbols used in this work can be found at the end of the appendix in Table 11.

A.1. Operator Splitting

We decompose the full operator, \mathcal{F} , into three components: advection (\mathcal{A}), diffusion(\mathcal{D}), and reaction(\mathcal{R}). To discretize the system for a time step Δt , we take N_{sub} sub-steps. At each sub-step l , we employ a first-order **Lie–Trotter operator-splitting** scheme to integrate the three operators sequentially. Each operator specializes in a specific physical regime:

1. **Transport stage (\mathcal{A})**. The Neural semi-Lagrangian (NSL) layer resolves the advective term $(\mathbf{u} \cdot \nabla) \mathbf{h}$. By back-tracing trajectories in latent space, the model preserves sharp gradients and phase information of synoptic systems that are often lost to numerical diffusion in purely grid-based CNNs.
2. **Dissipation stage (\mathcal{D})**. The spatial mixer emulates sub-grid scale diffusion and numerical stabilization. This stage provides the necessary smoothing to maintain physical consistency and prevent the accumulation of high-frequency noise.
3. **Reaction stage (\mathcal{R})**. Pointwise channel mixers handle the “Reaction” terms (non-linear interactions and source/sink terms, e.g., radiative cooling or latent heat release) that depend strictly on the local state variables rather than neighboring spatial information.

A.2. Forecast Pipeline

The PARADIS model predicts a forecast in 6-hour increments by providing a current \mathbf{q}_t and a previous 6-hour state \mathbf{q}_{t-1} via

$$\Delta \mathbf{q}_{t+1} = \text{PARADIS}(\mathbf{q}_t, \mathbf{q}_{t-1}), \quad (14)$$

which is executed through an encoder–processor–decoder pipeline. The following paragraphs outline this high-level information flow; a detailed breakdown of the internal operators and geometric constraints is provided in the subsequent sections of this Appendix.

Encoder (\mathcal{E}) The input feature vector $\mathbf{q} = [\mathbf{q}_t, \mathbf{q}_{t-1}]$, containing dynamic variables, static constants, and forcings, is projected into the latent space:

$$\mathbf{h}_0 = \mathcal{E}(\mathbf{q}_t, \mathbf{q}_{t-1}). \quad (15)$$

This stage initializes the latent PDE solver. By ingesting two historical time steps, the encoder provides the processor with the necessary temporal context to estimate the latent velocity field \mathbf{u}_l , effectively capturing the momentum and trend of the atmospheric flow.

Processor (\mathcal{P}) The processor evolves the hidden state \mathbf{h}_0 through N_{sub} successive layers, each approximating a fractional timestep of the total integration via the splitting scheme in Equation (3). This sub-stepping approach facilitates the learning of complex, long-range transport and non-linear interactions within a high-dimensional manifold

$$\mathbf{h}_{N_{\text{sub}}} = \mathcal{P}(\mathbf{h}_0) = (\mathcal{F}_{N_{\text{sub}}} \circ \cdots \circ \mathcal{F}_1)(\mathbf{h}_0). \quad (16)$$

The residual structure of these updates ensures that the network learns to compute local *tendencies*, improving training stability and gradient flow across the deep processor stack.

Decoder (\mathcal{G}) After N_{sub} integration steps, the final hidden state $\mathbf{h}_{N_{\text{sub}}}$ contains the accumulated tendencies. The decoder maps this representation back to the physical space to produce the forecast increment

$$\Delta \mathbf{q}_{t+1} = \mathcal{G}(\mathbf{h}_{N_{\text{sub}}}). \quad (17)$$

To ensure that the predicted increments are free from grid-scale artifacts, the decoder incorporates a final spatial mixing stage. The final prediction is then reconstructed as $\mathbf{q}_{t+1} = \mathbf{q}_t + \Delta \mathbf{q}_{t+1}$.

B. Model Architecture

The PARADIS architecture is designed to emulate an advection–diffusion–reaction process within a latent space. The overall design can be described as an encoder–processor–decoder structure. Let ϕ and λ be the latitude and longitude angles, respectively, of a spherical model of the Earth, i.e. $\mathbf{x} = \mathbf{x}(\phi, \lambda)$. This physical inspiration imposes hard constraints on layer behavior, ensuring the model evolves a high-dimensional representation $\mathbf{h}(\phi, \lambda) \in \mathbb{R}^C$ through components resembling partial differential equations (PDEs).

B.1. Composite Blocks

All stages in the PARADIS model are built from combinations of elementary linear operators: a *channel mixer*, which acts independently at each spatial location, a *spatial mixer*, which couples neighboring grid points through a separable convolution, and a bias term, which captures fine-scale detail required to better represent results. More complex blocks are formed by composing these operators and adding nonlinearities as well as learned bias terms.

B.1.1. CHANNEL MIXER

The channel mixer is a pointwise linear transformation that mixes feature channels without spatial coupling. It is implemented as a 1×1 convolution applied independently at each latitude–longitude location. It is defined by

$$\mathbf{h}_{\text{out}} = \mathbf{W}\mathbf{h}_{\text{in}} + \mathbf{b}, \quad (18)$$

where $\mathbf{W} \in \mathbb{R}^{C_{\text{out}} \times C_{\text{in}}}$ is a shared weight matrix and $\mathbf{b} \in \mathbb{R}^{C_{\text{out}}}$ is a learned bias. The number of trainable parameters in this layer is $(C_{\text{in}} + 1)C_{\text{out}}$, and is used throughout the network to change feature dimensionality and to couple latent channels.

B.1.2. SPATIAL MIXER

The spatial mixer introduces local spatial coupling while maintaining computational efficiency through a depthwise-separable convolution. This operation factorizes a standard convolution into a two-stage process that decouples spatial filtering from channel interaction. Formally, for an input latent field $\mathbf{h}_{\text{in}} \in \mathbb{R}^{C_{\text{in}} \times H \times W}$, we first apply geocyclic padding (Section J.1) to ensure continuity on the sphere. The mixer is then defined by

$$\mathbf{h}_{\text{out}} = \tilde{\mathbf{W}}(\mathbf{K}_d * \mathbf{h}_{\text{in}}) + \mathbf{b}, \quad (19)$$

where the operations are defined as follows

- Depthwise Convolution (\star): A channel-wise spatial filter $\mathbf{K}_d \in \mathbb{R}^{C_{\text{in}} \times k \times k}$ applied independently to each channel. This stage couples neighboring grid points within the same channel using a 3×3 kernel ($k = 3$), effectively acting as a learnable spatial stencil.

- Pointwise Projection: The channel mixer of Section B.1.1 with weights $\tilde{\mathbf{W}} \in \mathbb{R}^{C_{\text{out}} \times C_{\text{in}}}$ and bias $\mathbf{b} \in \mathbb{R}^{C_{\text{out}}}$ linearly recombines the spatially-filtered features.

By separating these steps, the mixer reduces the parameter count from $O(k^2 C_{\text{in}} C_{\text{out}})$ to $O(k^2 C_{\text{in}} + C_{\text{in}} C_{\text{out}})$. In total, the layer contains $9C_{\text{in}}$ parameters for the depthwise kernels and $(C_{\text{in}} + 1)C_{\text{out}}$ parameters for the subsequent channel-mixing projection.

B.1.3. LOW-RANK BIAS

To encode large-scale, spatially coherent corrections while maintaining parameter efficiency, PARADIS employs a low-rank factorization of a global bias field. Rather than store a full $C_{\text{out}} \times H \times W$ bias tensor, which is computationally expensive for high-dimensional latent spaces, we define a low-rank bottleneck with C_{in} channels and decompose it into a rank- K separable representation.

The core of this mechanism consists of three factor matrices: $\mathbf{A} \in \mathbb{R}^{C_{\text{in}} \times K}$ (per-channel coefficients), $\mathbf{U} \in \mathbb{R}^{K \times H}$ (latitudinal factors), and $\mathbf{V} \in \mathbb{R}^{K \times W}$ (longitudinal factors). An intermediate bias map $\mathbf{B}' \in \mathbb{R}^{C_{\text{in}} \times H \times W}$ is first reconstructed via a rank- K decomposition:

$$\mathbf{B}'_{c,i,j} = \sum_{k=1}^K \mathbf{A}_{ck} \mathbf{U}_{ki} \mathbf{V}_{kj}. \quad (20)$$

This intermediate field is then mapped to the target latent dimension C_{out} through a learned linear projection $\hat{\mathbf{W}} \in \mathbb{R}^{C_{\text{out}} \times C_{\text{in}}}$. The final bias field $\mathbf{B} \in \mathbb{R}^{C_{\text{out}} \times H \times W}$ is computed as:

$$\mathbf{B}_{o,i,j} = \sum_{c=1}^{C_{\text{in}}} \hat{\mathbf{W}}_{oc} \mathbf{B}'_{c,i,j}. \quad (21)$$

This two-stage approach provides a significant reduction in parameters, from $C_{\text{out}} \times H \times W$ down to $K(C_{\text{in}} + H + W) + C_{\text{out}}C_{\text{in}}$, while retaining the capacity to represent smooth, large-scale spatial patterns across the latent dimensions. By decoupling the spatial rank of the bias from the total number of latent channels, the model can efficiently incorporate spatially coherent, channel-specific corrections throughout the model. We use $K = 128$ by default.

B.1.4. NORMALIZATION LAYER

PARADIS employs a channel-wise normalization operator, referred to as *Channel Norm*, which is equivalent to applying Layer Normalization across the latent channel dimension at each spatial location. For an input field $\mathbf{x}(\phi, \lambda) \in \mathbb{R}^C$, *Channel Norm* normalizes each latent vector independently, without coupling statistics across space or batch elements.

Formally, the normalized latent state $\hat{\mathbf{h}}$ is given by

$$\hat{\mathbf{h}} = \gamma \odot \frac{\mathbf{h} - \mu}{\sqrt{\sigma^2 + \varepsilon}} + \beta, \quad (22)$$

where μ and σ^2 are the mean and variance computed across the channel dimension C , and $\{\gamma, \beta\} \in \mathbb{R}^C$ are learned affine parameters. A small constant ε is added for numerical stability. This results in affine parameters with $2C$ degrees of freedom.

This form of normalization is standard in attention-based and graph neural network architectures, where each spatial location (or token) is normalized independently in latent space. It is used throughout PARADIS to stabilize training while preserving local spatial structure.

B.2. Neural semi-Lagrangian Advection

Advection is the fundamental process by which atmospheric properties, such as heat, moisture, and momentum, are transported by the fluid flow. In global weather dynamics, the accurate representation of this transport is critical, as it governs the movement of synoptic systems across the sphere. While standard convolutional layers are restricted by local receptive fields, the *Neural semi-Lagrangian* layer explicitly models this long-range transport in latent space by solving the advection equation. Given a velocity field $\mathbf{u} = (u, v)$ and a time step Δt , the layer computes the advected state $\mathcal{A}_{\Delta t}(\mathbf{h}; \mathbf{u})$ by sampling \mathbf{h} at departure points traced backward along characteristics.

Latent Space Projection. To balance computational expressivity with memory efficiency, advection is performed in a reduced latent subspace of dimension $V < C$. This is in line with the idea that more than a single feature must likely travel with the same velocity field. We define a learned channel-wise down-projection $\mathcal{P}_\downarrow : \mathbb{R}^C \rightarrow \mathbb{R}^V$ and a corresponding lifting operator $\mathcal{P}_\uparrow : \mathbb{R}^V \rightarrow \mathbb{R}^C$. The advection step is applied to the projected state \mathbf{z}

$$\mathbf{z} = \mathcal{P}_\downarrow(\mathbf{h}), \quad \mathbf{h}_{\text{adv}} = \mathcal{P}_\uparrow(\tilde{\mathbf{z}}). \quad (23)$$

This projection allows the model to identify the most salient features for transport, effectively decoupling the advective dynamics from the full hidden state dimensionality.

Pole Continuity and Geometric Constraints. The latitude–longitude representation possesses singularities at the poles where meridians converge. To ensure the latent state remains single-valued at the poles and to prevent numerical instabilities, we enforce a zonal mean constraint at this location

$$\mathbf{z}_{c,i}^{\text{pole}} = \frac{1}{W} \sum_{j=0}^{W-1} \mathbf{z}_{c,i,j}, \quad i \in 0, H-1. \quad (24)$$

By applying this pole constraint both before and after the advection interpolation step, we filter out spurious high-frequency longitudinal noise that typically accumulates near the poles in grid-based transport schemes.

Spherical backtracing via rotated coordinates. Standard planar backtracing ($\mathbf{x}_d = \mathbf{x}_a - \mathbf{u}\Delta t$) introduces significant metric distortion near the poles. Following (McDonald & Bates, 1989), we compute departure points (ϕ_d, λ_d) by treating the local displacement as a rotation on the unit sphere. For an arrival point (ϕ_a, λ_a) , we define local angular displacements $\phi' = -v\Delta t$ and $\lambda' = -u\Delta t$. The departure coordinates are derived via spherical trigonometry

$$\phi_d = \arcsin(\sin \phi' \cos \phi_a + \cos \phi' \cos \lambda' \sin \phi_a), \quad (25)$$

$$\lambda_d = \lambda_a + \text{atan2}(\cos \phi' \sin \lambda', \cos \phi' \cos \lambda' \cos \phi_a - \sin \phi' \sin \phi_a). \quad (26)$$

This formulation ensures that the trajectory remains valid across the entire sphere, including the polar regions.

Differentiable Sampling and Interpolation. The calculated departure coordinates (ϕ_d, λ_d) are mapped to continuous grid indices (x, y) . The advected state $\tilde{\mathbf{z}}$ is then obtained via

$$\tilde{\mathbf{z}} = \mathcal{I}(\mathbf{z}^{\text{pad}}, \phi_d, \lambda_d), \quad (27)$$

where \mathcal{I} denotes a bicubic interpolation kernel, implemented in PyTorch via `grid_sample`.

B.3. Diffusion and Reaction Terms

B.3.1. DIFFUSION

The diffusion operator \mathcal{D}_{net} models local spatial mixing and sub-grid dissipation. It utilizes a spatial mixer (Section B.1.2) preceded by channel-wise normalization to stabilize the learned dissipation rates. The diffusion update is defined as

$$\mathbf{h}_{\text{diff}} = \mathcal{D}_{\text{net}}(\mathbf{h}) = \text{SpatialMixer}(\mathbf{h}) + \mathbf{B}_g, \quad (28)$$

where \mathbf{B}_g is the low-rank global bias field. This structure allows the model to represent anisotropic diffusion patterns that vary spatially and across latent channels.

B.3.2. REACTION

The reaction operator handles pointwise non-linear transformations and source/sink terms. It is implemented as a two-layer channel-mixer, acting independently at each spatial location, with a low-rank bias injected into the hidden state to provide spatially coherent corrections. The reaction mapping is given by

$$\mathbf{z} = \mathbf{W}_1 \mathbf{h} + \mathbf{b}_1 + \mathbf{B}_g, \quad (29a)$$

$$\mathbf{h}_{\text{react}} = \mathbf{W}_2 \text{SiLU}(\mathbf{z}) + \mathbf{b}_2, \quad (29b)$$

where $\mathbf{W}_1 \in \mathbb{R}^{C_h \times C}$ and $\mathbf{W}_2 \in \mathbb{R}^{C \times C_h}$ are channel-wise linear operators, and C_h denotes the hidden dimension for the channel mixers. By incorporating \mathbf{B}_g before the non-linearity, the model can learn spatially-varying reaction rates.

B.4. Feature Encoding

B.4.1. ENCODER

Let $\mathbf{x}(\phi, \lambda) \in \mathbb{R}^{C_{\text{input}}}$ denote the assembled input feature vector at grid location (ϕ, λ) (see Table 5 in the Appendix for a list of these input variables). The encoder maps these physical features into latent space $\mathbf{h} \in \mathbb{R}^C$. This projection is implemented as a sequence of pointwise channel mixers. For the single-layer case, which we apply in our work, the mapping is defined as

$$\mathbf{h}(\phi, \lambda) = \mathbf{W}_{\text{enc}} \mathbf{x}(\phi, \lambda), \quad (30)$$

where $\mathbf{W}_{\text{enc}} \in \mathbb{R}^{C \times C_{\text{in}}}$. By applying this transformation independently at each spatial location, the encoder initializes the latent representation while strictly preserving the local spatial structure of the input fields. No nonlinearity and no additive bias are used in this layer.

B.4.2. DECODER

The decoding stage recovers physical-space forecast increments from the final latent representation \mathbf{h}_N . To ensure that the predicted increments account for local spatial gradients, the decoder combines a spatial mixer with a final channel-wise projection. The decoding operation is defined as a two-stage transformation

$$\mathbf{h}_{\text{out}} = \text{SpatialMixer}(\mathbf{h}_N) + \mathbf{B}_g, \quad (31a)$$

$$\Delta \mathbf{q}(\phi, \lambda) = \mathbf{W}_{\text{dec}} \mathbf{h}_{\text{out}}(\phi, \lambda) + \mathbf{b}_{\text{dec}}, \quad (31b)$$

where $\mathbf{W}_{\text{dec}} \in \mathbb{R}^{C_{\text{out}} \times C}$ is a learned linear operator that maps the C latent channels back to the C_{out} physical dimensions. By applying a spatial mixer (Section B.1) immediately before the final projection, the decoder can smooth potential grid-scale artifacts and capture local spatial correlations that may have developed during the latent evolution. No additional non-linearities are applied in this stage, ensuring that $\Delta \mathbf{q}$ represents a direct linear decoding of the final processed features. The resulting increment is subsequently added to the current state \mathbf{q}_t to produce the final forecast.

C. Training Details

C.1. Training objective

Training is performed by minimizing a *reversed Huber* (also known as BerHu) loss, which combines linear behavior for small errors with quadratic behavior for large errors. Given a prediction \hat{y} and a reference value y , and a scale parameter $\delta > 0$, the loss is defined as

$$L_\delta(y, \hat{y}) = \begin{cases} \delta |y - \hat{y}|, & |y - \hat{y}| \leq \delta, \\ \frac{1}{2}(y - \hat{y})^2 + \frac{1}{2}\delta^2, & |y - \hat{y}| > \delta. \end{cases} \quad (32)$$

In contrast to the classical Huber loss (Huber, 1992), which is quadratic near the origin and linear for large errors, the reversed Huber loss enforces linear behavior for small residuals while penalizing large errors quadratically. The construction satisfies the following requirements

- (i) linear growth for small errors,
- (ii) quadratic growth for large errors,
- (iii) continuity at the transition point $|y - \hat{y}| = \delta$.

The reversed Huber loss is non-negative, convex, and satisfies $L_\delta(y, y) = 0$. Its gradient with respect to the prediction \hat{y} is given by

$$\frac{\partial L_\delta}{\partial \hat{y}} = \begin{cases} -\delta \text{ sign}(y - \hat{y}), & |y - \hat{y}| \leq \delta, \\ -(y - \hat{y}), & |y - \hat{y}| > \delta. \end{cases} \quad (33)$$

The gradient is discontinuous at $|y - \hat{y}| = \delta$, which may hinder numerical optimization.

To mitigate this issue, we employ a smooth approximation referred to as the *pseudo-reversed Huber loss*. Let $e = y - \hat{y}$ denote the prediction error. The smoothed loss is defined as

$$\tilde{L}_\delta(e) = (1 - w(e)) \delta|e| + w(e) \frac{1}{2}e^2, \quad (34)$$

where $w(e)$ is a sigmoid weighting function,

$$w(e) = \frac{1}{1 + \exp(-2(|e| - \delta))}. \quad (35)$$

This formulation replaces the sharp transition at $|e| = \delta$ with a smooth interpolation between the linear and quadratic regimes. The resulting loss is differentiable everywhere and remains convex.

The gradient of the pseudo-reversed Huber loss with respect to \hat{y} is

$$\frac{\partial \tilde{L}_\delta}{\partial \hat{y}} = -\delta \text{sign}(e)(1 - w(e)) - e w(e) - \left(\frac{1}{2}e^2 - \delta|e|\right) \frac{\partial w}{\partial \hat{y}}, \quad (36)$$

with

$$\frac{\partial w}{\partial \hat{y}} = -\frac{2 \text{sign}(e) \exp(-2(|e| - \delta))}{(1 + \exp(-2(|e| - \delta)))^2}. \quad (37)$$

The asymptotic behavior of \tilde{L}_δ matches that of the original reversed Huber loss:

- for $|e| \ll \delta$, $w(e) \approx 0$ and $\tilde{L}_\delta(e) \approx \delta|e|$;
- for $|e| \gg \delta$, $w(e) \approx 1$ and $\tilde{L}_\delta(e) \approx \frac{1}{2}e^2$.

The total training loss is obtained by applying \tilde{L}_δ independently to each predicted variable and pressure level, followed by a weighted aggregation. To this end, we make use of latitude and pressure-level weights described as follows.

C.1.1. INTEGRATION WEIGHTS

To ensure our metrics reflect physical reality across the global domain and vertical direction, we apply a dual weighting strategy for spatial and vertical dimensions.

Latitude weighting. Since the grid cells on a regular latitude-longitude grid decrease in area toward the poles, we apply latitude weights w_i to prevent over-representing polar regions. Following the methodology in Weatherbench (Rasp et al., 2024b), we define these weights to account for the integration of area on a sphere:

$$w_i \propto \begin{cases} \sin^2\left(\frac{\Delta\phi}{4}\right) & \text{if } \phi_i = \pm 90^\circ \text{ (poles),} \\ \cos(\phi_i) \sin\left(\frac{\Delta\phi}{2}\right) & \text{otherwise} \end{cases} \quad (38)$$

These weights are normalized to have a unit mean across the latitude dimension, ensuring that the magnitude of the loss metric remains comparable across different grid resolutions.

Pressure-level weighting. In addition to spatial weighting, we apply pressure-level weights v_k when aggregating metrics across multiple atmospheric layers. This ensures that the evaluation is dominated by the troposphere, where the majority of the atmospheric mass and weather phenomena reside, and maintains a meaningful contribution from the upper atmosphere. Following Lang et al. (2024b), the weight for a given pressure level p_k (expressed in hPa) is defined via

$$v_k = \max\left(\frac{p_k}{1000}, 0.2\right), \quad (39)$$

This linear scaling assigns higher importance to levels near the surface and applies a constant floor for levels above 200 hPa to prevent the stratosphere from being excessively disregarded in the loss function.

Variable (feature) weighting. We adopt a uniform weighting strategy across all physical output variables. While spatial and vertical weights account for the Earth’s geometry and atmospheric mass distribution, the relative contribution of each prognostic variable—such as geopotential, temperature, specific humidity, and wind components—to the aggregate skill scores is considered equal for the purposes of the integration of the loss function.

C.2. Optimization

We train PARADIS using the AdamW optimizer (Loshchilov & Hutter, 2017), which decouples weight decay from the gradient update to ensure more effective regularization of the latent weights. We use a base learning rate of 2.5×10^{-4} with momentum hyperparameters $\beta_1 = 0.9$ and $\beta_2 = 0.95$. A weight decay coefficient of 10^{-2} is applied. We maintain the maximum representational capacity of the high-dimensional latent space, and do not employ any sort of dropout mechanism. Furthermore, we find that the structural architecture of PARADIS did not require any global gradient clipping for stabilization during any of the training phases.

C.3. List of Hyperparameters

Key architectural and training hyperparameters are listed in Table 2, with total trainable parameter counts described in Table 3. Note that explicit advection only accounts for 25% of the total number of parameters.

Table 2. Hyperparameters and training configuration for PARADIS.

Category	Hyperparameter	Value
Model Architecture	Latent dimension (C)	1024
	Number of processor layers (N_{sub})	8
	Velocity subspace vectors (C_{adv})	256
	Bias latent channels (C_{in})	4
	Advection interpolation	Bicubic
	Encoder layers	1
	Bias rank	128
Training & Optimization	Time-history inputs	2
	Training steps	300,000
	Learning rate	2.5×10^{-4}
	Optimizer	AdamW
	Weight decay	10^{-2}
	Betas (β_1, β_2)	0.9, 0.95
	Loss function	Reversed Huber
	Huber delta (δ)	1.0
	Scheduler	WSD
	Warmup steps (Phase 1)	1,000
Dataset & Compute	Decay period	20%
	Time resolution	6h
	Spatial resolution	1.0°
	Vertical levels	13
	Global batch size	32
	Total number of input features	216
	Automatic mixed precision (AMP)	Enabled (bf16)

C.4. Training Curriculum

PARADIS is trained using a three-phase curriculum designed to (i) stabilize single-step dynamics learning, (ii) progressively improve multi-step forecast skill under an autoregressive (AR) rollout, and (iii) restore physical energy and small-scale detail through spectral fine-tuning. Phase 1 trains a one-step model (6-hour predictions) on ERA5 (1990–2019) with validation on 2020.

Following this initial stabilization, the model undergoes autoregressive fine-tuning in Phase 2 to mitigate exposure bias. Finally, Phase 3 employs a spectral curriculum using an adjusted mean square loss to counteract the double penalty effect and prevent the “blurring” typically associated with grid-point optimization. We discuss the curricula associated with each of these phases in the following sections, and present a summary in Table 4, Figure 8, and Section C.4.

Table 3. Parameter count for the different modules in PARADIS.

Module	Component	Parameters	%
Advection	Velocity net	4,862,976	13.1%
	SL advection	4,206,592	11.4%
	<i>Subtotal</i>	9,069,568	24.5%
Diffusion	Spatial mixer	73,728	0.2%
	Channel mixer	8,396,800	22.7%
	ChannelNorm	16,384	0.0%
	Bias	590,848	1.6%
	<i>Subtotal</i>	9,077,760	24.5%
Reaction	Channel mixer	16,793,600	45.4%
	ChannelNorm	16,384	0.0%
	Bias	590,848	1.6%
	<i>Subtotal</i>	17,400,832	47.0%
Encoding	Input	221,184	0.6%
	Output	1,233,122	3.3%
	<i>Subtotal</i>	1,454,306	3.9%
Total		37,002,466	100.0%

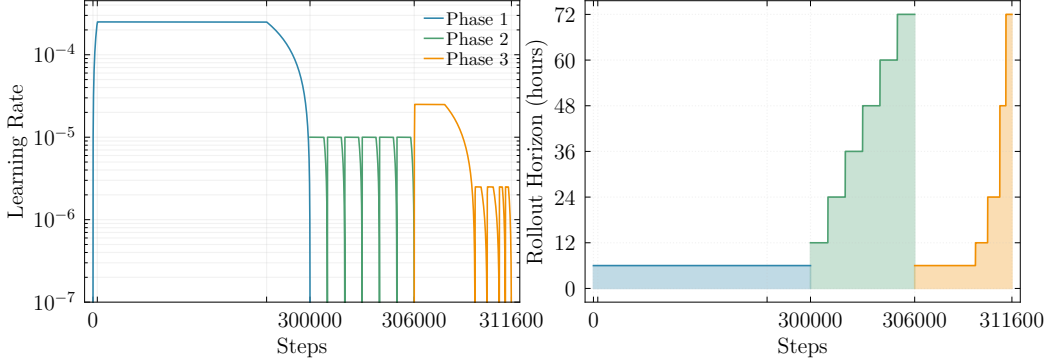


Figure 8. Curriculum detail showing steps and learning rate throughout training and finetuning phases.

C.4.1. PHASE 1: LEARNING RATE SCHEDULE

In Phase 1 we train for a total of $3 \cdot 10^5$ batch-size 32 updates with a base learning rate of 2.5×10^{-4} and employ a Warmup-Steady-Decay (WSD) learning-rate scheduler. The WSD scheduler (Hu et al., 2024) performs

- a short warmup to avoid early optimization instabilities when gradients and activation statistics are still settling, followed by
- a stable phase where the learning rate is maintained constant and covers the majority of the training time,
- and a step-like decay to reduce the learning rate once the model has reached a stable training regime.

Concretely, we warm up for 1000 steps and then apply a multiplicative decay period of 0.2 (i.e., dropping the learning rate during 20% of the training schedule).

C.4.2. PHASE 2: AUTOREGRESSIVE TRAINING

Phase 2 fine-tunes the model for multi-step forecasting using autoregressive rollouts. We initialize this phase from the Phase 1 checkpoint and employ a curriculum-based training strategy consisting of six stages. In each stage, the rollout horizon is incrementally increased by 12 hours (2 steps) until a maximum window of 72 hours (12 steps) is reached.

During an autoregressive step, the model produces a sequence of N_{rollout} predictions $(\mathbf{q}_{t+1}, \mathbf{q}_{t+2}, \dots, \mathbf{q}_{t+N_{\text{rollout}}})$ conditioned on the current inputs. Losses are accumulated across all predicted lead times in the rollout, and we backpropagate through

the full unrolled trajectory down to the initial state q_t . This process enforces consistency of the learned dynamics under repeated application and mitigates exposure bias relative to one-step training. For Phase 2, we utilize a smaller learning rate of 10^{-5} to preserve the single-step skill while adapting to long-horizon behavior. We again employ the WSD scheduler with zero warmup and a 20% decay, as the optimization is already in a stable regime.

C.4.3. PHASE 3: SPECTRAL FINETUNING

The final stage of our training pipeline addresses the double penalty effect (Subich et al., 2025), a fundamental limitation in deterministic weather forecasting where the use of traditional grid-point losses often results in blurry or overly smooth fields. To counteract this, we fine-tune the model using an adjusted mean square error (AMSE) loss function. This loss operates in the spherical harmonic domain to separately penalize phase and amplitude (energy) errors when modes are grouped by total wavenumber, encouraging the model to predict a realistic energy cascade even in the limit of unpredictable phases (positioning), which naturally happens at longer lead times.

We employ a progressive spectral curriculum adapted from (Subich et al., 2025) to stabilize training as rollout complexity increases, structured into the following substages

- Fine-tuning is divided into five stages with increasing forecast horizons of 1, 2, 4, 8, and 12 six-hour steps. Each stage is initialized from the previous checkpoint to carry forward learned spectral corrections.
- The training duration decreases as the rollout horizon grows. We perform 3500 steps for the first stage (1-step rollout), 700 steps for the next two stages (2 and 4-step rollouts), and finalize with 350 steps for the remaining stages (8 and 12-step rollouts).
- We utilize a base learning rate of 2.5×10^{-5} for the initial 1-step rollout. For all subsequent multi-step stages, the rate is reduced to 2.5×10^{-6} to preserve stability during autoregressive integration.
- A WSD scheduler is applied at each stage with a 50% decay period. The number of warmup steps (n) is reduced progressively across the curriculum, moving from 128 steps for the first stage down to 25 steps for the final 12-step rollout.

Table 4. Unified Training Curriculum for PARADIS. The schedule details the progression from single-step stabilization (Phase 1) to multi-step autoregressive fine-tuning (Phase 2) with a 12-hour incremental window, and final spectral refinement (Phase 3). *Max steps* refers to the number of optimizer updates with a batch size of 32.

Phase	Stage	Rollout Steps	Horizon	Max Steps	Learning Rate	Warmup	Decay Period
Phase 1	Initial	1	6h	300,000	2.5×10^{-4}	1,000	0.2
	AR Stage 1	2	12h	1,000	1.0×10^{-5}	0	0.2
	AR Stage 2	4	24h	1,000	1.0×10^{-5}	0	0.2
	AR Stage 3	6	36h	1,000	1.0×10^{-5}	0	0.2
	AR Stage 4	8	48h	1,000	1.0×10^{-5}	0	0.2
	AR Stage 5	10	60h	1,000	1.0×10^{-5}	0	0.2
	AR Stage 6	12	72h	1,000	1.0×10^{-5}	0	0.2
Phase 2	Spectral 1	1	6h	3,500	2.5×10^{-5}	128	0.5
	Spectral 2	2	12h	700	2.5×10^{-6}	50	0.5
	Spectral 3	4	24h	700	2.5×10^{-6}	50	0.5
	Spectral 4	8	48h	350	2.5×10^{-6}	25	0.5
	Spectral 5	12	72h	350	2.5×10^{-6}	25	0.5

C.4.4. EFFECT OF CURRICULUM STAGES ON FORECAST SKILL

The effect of the multi-stage training curriculum on forecast behavior is summarized in Figures 9 and 10. Together, these diagnostics isolate how each training phase influences pointwise accuracy, long-horizon stability, and spectral structure.

Figure 9 shows the evolution of RMSE as a function of forecast lead time for models obtained after Phase 1, Phase 2, and Phase 3. After Phase 1, forecast error grows rapidly with lead time, reflecting limited robustness under autoregressive rollout

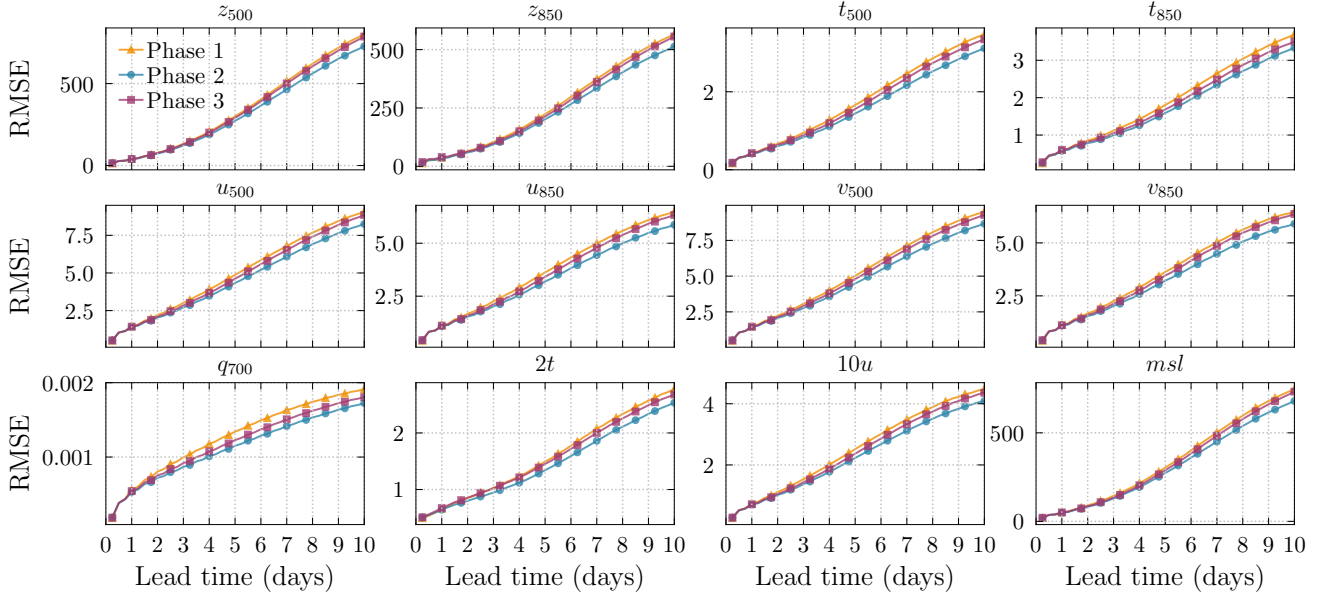


Figure 9. Evolution of RMSE (lower is better) as a function of forecast lead time for PARADIS after Phase 1, Phase 2, and Phase 3 training. Each panel corresponds to a different atmospheric variable. Autoregressive fine-tuning (Phase 2) substantially reduces long-range error growth across variables, while spectral fine-tuning (Phase 3) does not optimize for RMSE and hence a small deterioration is the price of improved spectral accuracy.

despite strong single-step performance. Autoregressive fine-tuning in Phase 2 substantially reduces long-range error growth across all variables, demonstrating that exposure to multi-step rollouts is essential for learning stable long-horizon dynamics.

Phase 3 introduces a targeted trade-off. As shown in Figure 9, spectral fine-tuning leads to a modest increase in RMSE relative to the Phase 2 model. This behavior is expected, as Phase 3 no longer optimizes a grid-point RMSE objective but instead prioritizes spectral consistency through the AMSE loss. In this regime, the model is encouraged to maintain realistic energy distributions across scales rather than minimizing pointwise error, particularly at small spatial scales where phase uncertainty is unavoidable at long lead times.

The benefits of this trade-off are evident in the spectral diagnostics. Figure 10 shows that Phase 3 substantially restores small-scale energy, with amplitude ratios remaining closer to unity at high wavenumbers compared to earlier phases. Coherence diagnostics further indicate that these gains are not achieved by sacrificing large-scale phase alignment. Together, these results indicate that spectral fine-tuning selectively counteracts diffusion-induced smoothing accumulated during autoregressive integration, at the cost of a controlled increase in RMSE. The model obtained after Phase 3 is referred to as PARADIS-AMSE elsewhere in this work. Compared to the Phase 2 model, PARADIS-AMSE exhibits improved multiscale structure and physically consistent energy spectra, while retaining competitive long-range forecast skill.

Overall, the curriculum enables PARADIS to first learn stable short-range dynamics, then robust long-horizon autoregressive behavior, and finally physically meaningful multiscale structure. The observed trade-offs between RMSE and spectral fidelity highlight the importance of aligning the training objective with the desired physical properties of long-range weather forecasts.

C.4.5. COMPUTE DETAILS

The PARADIS model was trained on a distributed infrastructure comprising 32 NVIDIA H100 GPUs. We utilized Distributed Data Parallelism for inter-node communication and employed Automatic Mixed Precision (AMP) with the `bf16` data format to optimize numerical performance and memory efficiency.

Phase 1 training, which involved $3 \cdot 10^5$ optimization steps at 1° resolution with a global batch size of 32, was completed in 19 hours. This represents a total computational cost of approximately 608 GPU-hours and a training throughput of roughly 4.38 steps per second. The finetuning phases had a cost of 30 GPU-hours for Phase 2 and 10 GPU-hours for Phase 3. While GraphCast required roughly 4 weeks on 32 Cloud TPU v4 devices (Lam et al., 2023) due to the 0.25° resolution, PARADIS

achieves competitive skill with only 608 GPU-hours on H100s. This represents an order-of-magnitude reduction in training energy. Inference cost scales predictably with grid resolution. On a single H100, a full 10-day autoregressive rollout takes 1.31 s at 2° , 3.35 s at 1° , and 55.78 s at 0.25° . As expected, runtime increases steeply with finer grids due to the larger number of spatial degrees of freedom, while remaining in the sub-minute regime even at 0.25° .

To manage the memory footprint of our non-hierarchical architecture during the autoregressive fine-tuning stages (Phases 2 and 3), gradient checkpointing was enabled. This was a critical requirement for backpropagating through long-horizon rollouts of up to 12 steps, as it allowed the 1024-dimensional latent space and full-resolution grid to fit within the H100 device memory without resorting to spatial downsampling.

D. Datasets

D.1. Training Dataset: ECMWF's ERA5

For training and evaluation, we employed ECMWF's ERA5 reanalysis, which delivers a high-resolution global reconstruction of the atmospheric state from 1959 onward. ERA5 is generated using the HRES model within ECMWF's 4D-Var assimilation framework (Andersson & Thépaut, 2008), combining observations over 12-hour windows with short-range forecasts. The dataset provides hourly output at 0.25° resolution.

Our study uses a tailored subset spanning 1990-01-01 to 2019-12-31, downsampled to four synoptic times per day (00, 06, 12, and 18 UTC). All fields were taken by directly sampling the synoptic times from the dataset. The selected configuration includes surface variables and 13 pressure levels: 50, 100, 150, 200, 250, 300, 400, 500, 600, 700, 850, 925, and 1000 hPa.

To ensure efficiency during training, the dataset was directly obtained from WeatherBench (Rasp et al., 2024a), reprocessed, and stored in re-chunked form along the time dimension to reduce random-access overhead.

Table 5. Input and output variable inventory for the PARADIS model. Atmospheric variables are evaluated at 13 pressure levels (50, 100, 150, 200, 250, 300, 400, 500, 600, 700, 850, 925, 1000 hPa).

Category	Variable Name	Input	Output
Atmospheric	Geopotential	✓	✓
	Cartesian horizontal wind vector	✓	✓
	Specific humidity	✓	✓
	Temperature	✓	✓
	Vertical velocity	✓	✓
Surface	10m Cartesian horizontal wind vector	✓	✓
	2m Temperature	✓	✓
	Mean sea-level pressure	✓	✓
	Surface pressure	✓	✓
	Total column water	✓	✓
Forcings	TOA incident solar radiation	✓	✗
	Time of day (sin, cos)	✓	✗
	Year progress (sin, cos)	✓	✗
Constants	Geopotential at surface	✓	✗
	Land-sea mask	✓	✗
	Topographic slope	✓	✗
	Sub-grid topographic standard deviation	✓	✗
	Inverse longitude spacing	✓	✗
	Latitude / longitude	✓	✗
	$\cos(\phi)$	✓	✗
	$\sin(\lambda), \cos(\lambda)$	✓	✗

D.2. Evaluation Datasets

To benchmark the performance of the PARADIS model, we compare our forecasts against both traditional numerical weather prediction (NWP) systems and state-of-the-art data-driven models. Forecasts for these baseline models were downloaded from the WeatherBench repository.

- **ECMWF HRES:** We utilize the High-Resolution operational forecasts from the European Centre for Medium-Range Weather Forecasts (ECMWF) Integrated Forecasting System (IFS). This provides a baseline representing the current operational standard in deterministic physics-based forecasting.
- **GraphCast:** We include forecasts from GraphCast (Lam et al., 2023), a 0.25° machine learning model based on graph neural networks. These outputs are sourced from the WeatherBench 2 archive (Rasp et al., 2024b) to compare PARADIS against a leading model that uses a multiscale mesh representation.
- **Pangu-Weather:** We benchmark against Pangu-Weather (Bi et al., 2023), which employs a 3D Earth-Specific Transformer. This comparison is particularly relevant as Pangu-Weather uses hierarchical structures, whereas PARADIS remains non-hierarchical at full grid resolution.
- **Climatology and Persistence:** Standard reference baselines, including a 30-year climatology derived from ERA5 and a persistence forecast, are used to evaluate the forecast skill and energy retention of the model over extended lead times.

Table 6. Variable reference: short names and long names for meteorological fields used in PARADIS evaluation.

Category	Short Name	Long Name
Atmospheric	z	Geopotential
	t	Temperature
	u	u -component of wind (zonal)
	v	v -component of wind (meridional)
	q	Specific humidity
Surface	$2t$	2-metre temperature
	$10u$	10-metre u -component of wind
	msl	Mean sea-level pressure

Short and long names of evaluated variables are listed in Table 6.

D.3. Data Normalization

Normalization is a key step in preparing data for machine learning. It scales features to a similar range, making predictive models more accurate and reliable. Different normalization strategies are chosen based on the physical characteristics of the variables. For most atmospheric variables, such as temperature, wind components, and geopotential, we compute the mean and standard deviation independently at each pressure level. Then, Z-score normalization is applied as follows

$$q_{\text{normalized}} = \frac{q - \mu(q)}{\sigma(q)}. \quad (40)$$

Here, $\mu(q)$ and $\sigma(q)$ represent the mean and standard deviation of the variable q for a given pressure level.

E. Verification Strategies

To assess the performance of the PARADIS model, we employ a suite of metrics that evaluate the forecast accuracy in both physical and spectral space.

E.1. RMSE Skill

The RMSE provides a measure of the average magnitude of the forecast error. To account for the convergence of meridians toward the poles, we utilize an area-weighted RMSE

$$\text{RMSE}(t) = \sqrt{\frac{1}{\sum_{i,j} w_i} \sum_{i=1}^H \sum_{j=1}^W w_i (\hat{y}_{i,j}(t) - y_{i,j}(t))^2}, \quad (41)$$

where \hat{y} and y are the predicted and ground-truth fields, respectively. The weight w_i corresponds to that of the latitude ϕ_i at grid row i . This weighting ensures that errors near the equator (which represent a larger physical area) are prioritized appropriately. These weights are computed according to (Rasp et al., 2024b; Lam et al., 2023) for datasets containing the poles.

E.2. ACC skill

The anomaly correlation coefficient (ACC) measures the spatial similarity between the predicted and observed anomalies (deviations from the long-term climatology). It is highly sensitive to the phase and structure of weather systems. Following (Rasp et al., 2024b)

$$\text{ACC}(t) = \frac{\sum_{i,j} w_i (f_{i,j}(t) \cdot o_{i,j}(t))}{\sqrt{\sum_{i,j} w_i (f_{i,j}(t))^2 \cdot \sum_{i,j} w_i (o_{i,j}(t))^2}}, \quad (42)$$

where $f = \hat{y} - \bar{y}$ and $o = y - \bar{y}$ are the predicted and observed anomalies relative to the climatological mean \bar{y} . An ACC of 1 indicates perfect spatial correlation, while a value of 0.6 is typically considered the threshold for a “useful” synoptic forecast (Murphy & Epstein, 1989).

E.3. Power Spectra

The amplitude ratio is the square root of the power spectral density ratio between the forecast and verifying analysis, where we add together all spherical harmonic modes of the same total wavenumber. Since the full power spectrum decays over several orders of magnitude from the synoptic scales to the finest scales, this normalization highlights the departure from the ground-truth reference and depicts the scale-dependent smoothing (or noise generation) of a model.

The spectral coherence is the correlation coefficient between the individual amplitudes of the forecast and the verifying ground truth, again grouped by total wavenumber. This shows the scale-dependent forecast skill, independently of smoothing.

For plotting purposes, these values are computed independently per forecast and then averaged over the 2020 verification period.

Given fixed forecast skill, MSE optimality is reached when a model’s smoothing (amplitude ratio) is equal to its coherence on a mode-by-mode basis, and a similar relationship holds under MAE-style loss functions with mild assumptions about distribution regularity. ML-based models such as PARADIS (stage 2), GraphCast, and Pangu-Weather approach this optimum ratio. The physics-based HRES baseline is designed to produce realistic forecast fields rather than to give an MSE-optimal forecast, so its amplitude ratio is approximately 1 for all modes.

F. Comparison with Baseline Models

We compare PARADIS against established numerical and machine-learning baselines, including HRES, GraphCast, and Pangu, using a controlled and resolution-aware evaluation protocol. PARADIS is trained and deployed at a native horizontal resolution of 1° . To ensure a fair comparison that isolates differences in the learned forecast operators rather than differences in grid spacing, our primary analysis evaluates all models on a common 1° grid. Forecasts produced at 0.25° resolution are regressed to 1° prior to evaluation, and all metrics are computed using identical verification procedures. We note that the relative improvement over HRES is consistent with other evaluation years, such as 2022, but data from all considered models were not available for a quantitative comparison for this year.

Baseline configurations. Baseline machine-learning models are evaluated using their publicly released configurations and pretrained weights, without retraining or restricting their input variables. This reflects their fully optimized operational usage and avoids introducing artificial handicaps. PARADIS is trained and evaluated using a comparable set of atmospheric state variables.

F.1. Forecast skill at Matched 1° Resolution.

Figure 11, Figure 12, and Table 7 report forecast skill as a function of lead time from 1 to 10 days for a range of atmospheric variables and pressure levels. Root mean square error (RMSE) and ACC are evaluated after mapping all models to a common 1° grid, isolating differences in the learned forecast operators from differences in spatial resolution.

Table 7. RMSE for selected atmospheric variables at multiple pressure levels, evaluated across forecast lead times of 1 to 10 days. Bold values denote the best-performing model for each variable, level, and lead time; underlined values denote the second-best.

Variable	Level	Model	1d	2d	3d	4d	5d	6d	7d	8d	9d	10d
z	500	HRES	4.38e+01	8.31e+01	1.38e+02	2.15e+02	3.09e+02	4.14e+02	5.24e+02	6.30e+02	7.21e+02	8.00e+02
		GraphCast	4.05e+01	<u>7.53e+01</u>	<u>1.20e+02</u>	<u>1.93e+02</u>	<u>2.75e+02</u>	<u>3.72e+02</u>	<u>4.71e+02</u>	<u>5.68e+02</u>	<u>6.54e+02</u>	<u>7.29e+02</u>
		Pangu	4.76e+01	8.41e+01	1.37e+02	2.09e+02	2.99e+02	3.99e+02	5.03e+02	6.08e+02	7.02e+02	7.84e+02
		PARÁDIS	3.94e+01	7.37e+01	1.23e+02	1.89e+02	2.73e+02	3.66e+02	4.65e+02	5.62e+02	6.51e+02	7.27e+02
		PARADIS AMSE	4.01e+01	7.68e+01	1.29e+02	2.01e+02	2.91e+02	3.93e+02	5.01e+02	6.05e+02	7.02e+02	7.87e+02
z	850	HRES	4.29e+01	7.11e+01	1.10e+02	1.64e+02	2.31e+02	3.05e+02	3.81e+02	4.53e+02	5.15e+02	5.69e+02
		GraphCast	3.68e+01	6.18e+01	9.82e+01	1.47e+02	2.08e+02	2.73e+02	<u>3.42e+02</u>	4.07e+02	4.65e+02	5.16e+02
		Pangu	4.14e+01	6.82e+01	1.06e+02	1.58e+02	2.22e+02	2.93e+02	3.65e+02	4.36e+02	4.99e+02	5.53e+02
		PARÁDIS	3.54e+01	5.94e+01	9.43e+01	1.42e+02	2.02e+02	2.67e+02	3.36e+02	4.03e+02	4.63e+02	5.13e+02
		PARADIS AMSE	3.99e+01	6.34e+01	9.91e+01	1.50e+02	2.14e+02	2.85e+02	3.62e+02	4.33e+02	4.99e+02	5.56e+02
z	1000	HRES	4.98e+01	8.04e+01	1.21e+02	1.78e+02	2.48e+02	3.25e+02	4.02e+02	4.76e+02	5.38e+02	5.92e+02
		GraphCast	4.18e+01	6.84e+01	1.07e+02	1.58e+02	2.22e+02	2.90e+02	3.61e+02	4.28e+02	4.87e+02	5.38e+02
		Pangu	4.68e+01	7.53e+01	1.16e+02	1.70e+02	2.37e+02	3.11e+02	3.85e+02	4.58e+02	5.22e+02	5.75e+02
		PARÁDIS	3.85e+01	6.51e+01	1.02e+02	1.53e+02	2.16e+02	2.84e+02	3.56e+02	4.25e+02	4.86e+02	5.37e+02
		PARADIS AMSE	4.08e+01	6.80e+01	1.07e+02	1.61e+02	2.28e+02	3.02e+02	3.82e+02	4.55e+02	5.22e+02	5.78e+02
t	500	HRES	4.76e-01	7.29e-01	1.01e+00	1.33e+00	1.70e+00	2.08e+00	2.48e+00	2.84e+00	3.15e+00	3.40e+00
		GraphCast	4.07e-01	<u>6.05e-01</u>	<u>8.39e-01</u>	<u>1.13e+00</u>	<u>1.46e+00</u>	<u>1.82e+00</u>	<u>2.18e+00</u>	<u>2.53e+00</u>	<u>2.83e+00</u>	<u>3.11e+00</u>
		Pangu	4.62e-01	6.54e-01	9.04e-01	1.21e+00	1.58e+00	1.96e+00	2.34e+00	2.73e+00	3.05e+00	3.33e+00
		PARÁDIS	4.10e-01	6.05e-01	8.34e-01	1.11e+00	1.44e+00	1.80e+00	2.17e+00	2.52e+00	2.84e+00	3.11e+00
		PARADIS AMSE	4.26e-01	6.39e-01	8.90e-01	1.19e+00	1.56e+00	1.95e+00	2.35e+00	2.74e+00	3.06e+00	3.35e+00
t	850	HRES	7.37e-01	1.03e+00	1.29e+00	1.59e+00	1.93e+00	2.32e+00	2.72e+00	3.10e+00	3.43e+00	3.70e+00
		GraphCast	5.66e-01	7.76e-01	9.97e-01	1.27e+00	1.61e+00	1.99e+00	2.37e+00	2.75e+00	3.10e+00	3.38e+00
		Pangu	6.78e-01	8.80e-01	1.11e+00	1.41e+00	1.76e+00	2.16e+00	2.56e+00	2.94e+00	3.29e+00	3.59e+00
		PARÁDIS	5.79e-01	7.86e-01	9.99e-01	1.26e+00	1.59e+00	1.96e+00	2.35e+00	2.71e+00	3.05e+00	3.33e+00
		PARADIS AMSE	6.03e-01	8.22e-01	1.05e+00	1.33e+00	1.68e+00	2.08e+00	2.49e+00	2.87e+00	3.22e+00	3.50e+00
t	1000	HRES	6.82e-01	9.03e-01	1.10e+00	1.33e+00	1.61e+00	1.92e+00	2.22e+00	2.52e+00	2.76e+00	2.96e+00
		GraphCast	5.56e-01	7.18e-01	8.93e-01	1.11e+00	1.38e+00	1.67e+00	1.98e+00	2.28e+00	2.55e+00	2.77e+00
		Pangu	6.43e-01	8.15e-01	1.01e+00	1.25e+00	1.53e+00	1.84e+00	2.16e+00	2.45e+00	2.71e+00	2.93e+00
		PARÁDIS	5.43e-01	7.15e-01	8.92e-01	1.10e+00	1.37e+00	1.66e+00	1.96e+00	2.24e+00	2.50e+00	2.71e+00
		PARADIS AMSE	5.74e-01	7.64e-01	9.57e-01	1.18e+00	1.47e+00	1.77e+00	2.09e+00	2.39e+00	2.64e+00	2.85e+00
q	500	HRES	4.18e-04	5.36e-04	6.18e-04	6.90e-04	7.55e-04	8.16e-04	8.74e-04	9.24e-04	9.69e-04	1.01e-03
		GraphCast	2.85e-04	3.80e-04	4.50e-04	5.14e-04	5.76e-04	6.37e-04	6.96e-04	7.49e-04	7.97e-04	8.38e-04
		Pangu	3.17e-04	4.16e-04	4.99e-04	5.78e-04	6.53e-04	7.25e-04	7.91e-04	8.50e-04	9.03e-04	9.46e-04
		PARÁDIS	2.93e-04	3.87e-04	4.56e-04	5.22e-04	5.87e-04	6.52e-04	7.14e-04	7.73e-04	8.24e-04	8.71e-04
		PARADIS AMSE	3.00e-04	4.05e-04	4.84e-04	5.58e-04	6.30e-04	7.02e-04	7.68e-04	8.28e-04	8.79e-04	9.24e-04
q	700	HRES	7.71e-04	1.01e-03	1.18e-03	1.33e-03	1.47e-03	1.59e-03	1.71e-03	1.81e-03	1.90e-03	1.97e-03
		GraphCast	5.19e-04	7.08e-04	8.50e-04	9.84e-04	1.11e-03	1.24e-03	1.36e-03	1.46e-03	1.56e-03	1.64e-03
		Pangu	5.97e-04	7.86e-04	9.50e-04	1.11e-03	1.26e-03	1.41e-03	1.54e-03	1.66e-03	1.77e-03	1.85e-03
		PARÁDIS	5.31e-04	7.21e-04	8.69e-04	1.01e-03	1.15e-03	1.29e-03	1.42e-03	1.53e-03	1.64e-03	1.72e-03
		PARADIS AMSE	5.42e-04	7.33e-04	8.91e-04	1.08e-03	1.23e-03	1.37e-03	1.51e-03	1.62e-03	1.73e-03	1.81e-03
v	850	HRES	1.03e-03	1.33e-03	1.52e-03	1.68e-03	1.83e-03	1.96e-03	2.08e-03	2.19e-03	2.28e-03	2.36e-03
		GraphCast	6.15e-04	8.44e-04	1.01e-03	1.16e-03	1.30e-03	1.45e-03	1.58e-03	1.70e-03	1.81e-03	1.90e-03
		Pangu	7.47e-04	9.60e-04	1.14e-03	1.30e-03	1.47e-03	1.63e-03	1.78e-03	1.91e-03	2.03e-03	2.13e-03
		PARÁDIS	6.37e-04	8.66e-04	1.03e-03	1.18e-03	1.33e-03	1.48e-03	1.62e-03	1.75e-03	1.86e-03	1.95e-03
		PARADIS AMSE	6.55e-04	9.04e-04	1.09e-03	1.25e-03	1.42e-03	1.58e-03	1.73e-03	1.86e-03	1.97e-03	2.06e-03
v	500	HRES	1.77e+00	2.60e+00	3.42e+00	4.32e+00	5.25e+00	6.21e+00	7.15e+00	8.00e+00	8.71e+00	9.32e+00
		GraphCast	1.42e+00	2.07e+00	2.76e+00	3.53e+00	4.38e+00	5.27e+00	6.15e+00	6.95e+00	7.64e+00	8.22e+00
		Pangu	1.59e+00	2.21e+00	2.95e+00	3.80e+00	4.73e+00	5.68e+00	6.59e+00	7.47e+00	8.25e+00	8.89e+00
		PARÁDIS	1.41e+00	2.04e+00	2.71e+00	3.48e+00	4.33e+00	5.21e+00	6.09e+00	6.91e+00	7.65e+00	8.25e+00
		PARADIS AMSE	1.43e+00	2.11e+00	2.85e+00	3.68e+00	4.62e+00	5.59e+00	6.53e+00	7.41e+00	8.19e+00	8.85e+00
v	1000	HRES	1.52e+00	2.13e+00	2.70e+00	3.32e+00	3.99e+00	4.65e+00	5.29e+00	5.85e+00	6.32e+00	6.68e+00
		GraphCast	1.10e+00	1.56e+00	2.06e+00	2.62e+00	3.25e+00	3.90e+00	4.49e+00	5.03e+00	5.67e+00	5.87e+00
		Pangu	1.29e+00	1.73e+00	2.25e+00	2.85e+00	3.52e+00	4.21e+00	4.84e+00	5.42e+00	5.93e+00	6.32e+00
		PARÁDIS	1.09e+00	1.54e+00	2.02e+00	2.57e+00	3.20e+00	3.83e+00	4.44e+00	5.00e+00	5.49e+00	5.87e+00
		PARADIS AMSE	1.16e+00	1.59e+00	2.12e+00	2.73e+00	3.42e+00	4.12e+00	4.79e+00	5.39e+00	5.92e+00	6.33e+00
v	1000	HRES	1.52e+00	2.11e+00	2.67e+00	3.30e+00	3.98e+00	4.66e+00	5.30e+00	5.87e+00	6.34e+00	6.71e+00
		GraphCast	1.10e+00	1.57e+00	2.07e+00	2.64e+00	3.27e+00	3.90e+00	4.53e+00	5.09e+00	5.52e+00	5.88e+00
		Pangu	1.30e+00	1.74e+00	2.26e+00	2.87e+00	3.56e+00	4.24e+00	4.89e+00	5.48e+00	5.96e+00	6.33e+00
		PARÁDIS	1.10e+00	1.55e+00	2.03e+00	2.59e+00	3.22e+00	3.85e+00	4.48e+00	5.07e+00	5.53e+00	5.90e+00
		PARADIS AMSE	1.12e+00	1.60e+00	2.13e+00	2.76e+00	3.46e+00	4.16e+00	4.86e+00	5.48e+00	5.97e+00	6.36e+00
w	500	HRES	1.22e+00	1.66e+00	2.10e+00	2.62e+00	3.18e+00	3.74e+00	4.28e+00	4.79e+00	5.19e+00	5.52e+00
		GraphCast	8.41e-01	1.20e+00	1.59e+00	2.06e+00	2.59e+00	3.12e+00	3.66e+00	4.14e+00</		

Across most variables and lead times, PARADIS achieves lower RMSE than the baseline models, with particularly consistent improvements for dynamically advected fields such as geopotential height and horizontal wind components. These gains indicate improved control of error growth during autoregressive rollouts. At the same time, PARADIS maintains higher ACC at longer lead times, demonstrating superior preservation of large-scale phase and spatial structure. The combination of reduced RMSE and sustained ACC suggests that improvements are not driven by excessive smoothing, but by more accurate long-range transport of coherent atmospheric features.

Importantly, these improvements are not confined to a small subset of variables or forecast horizons. Instead, PARADIS exhibits a systematic enhancement across the multivariate forecast state, reflecting improved global forecast dynamics rather than variable-specific tuning. The PARADIS-AMSE variant highlights the sensitivity of short-range RMSE to the training objective, while exhibiting similar long-range ACC behavior, reinforcing that the dominant gains arise from architectural structure rather than loss-function choice.

While the matched 1° evaluation removes fine-scale detail present at 0.25° , it isolates the quality of the learned forecast operators. At these scales, forecast error growth is dominated by large-scale transport and phase errors rather than small-scale variance, making RMSE and ACC together particularly informative metrics for assessing long-range dynamical fidelity.

F.2. Forecast Error Along the Vertical Direction

To assess whether improvements are confined to specific atmospheric layers, Figure 13 shows the vertical distribution of RMSE as a function of pressure level, aggregated across all lead times. PARADIS reduces error throughout the troposphere and lower stratosphere for the evaluated variables. This vertical consistency suggests that the benefits of explicit transport propagate coherently through the full three-dimensional atmospheric column, rather than being restricted to surface-level or upper-level fields. In particular, improvements in mid-tropospheric winds and geopotential height indicate enhanced representation of large-scale dynamical structures.

F.3. Spectral Fidelity and Phase Coherence.

Pointwise error metrics alone do not fully capture whether a model preserves physically meaningful multiscale structure during autoregressive rollouts. We therefore evaluate spectral characteristics using amplitude ratios and coherence as functions of spherical wavenumber (Figures 14 and 15). PARADIS exhibits reduced spectral roll-off at high wavenumbers, with amplitude ratios remaining closer to unity across lead times, indicating improved retention of small-scale energy. Mode-by-mode spectral coherence compares the forecast and truth in spherical harmonic space and does not depend on whether one model is nominally trained at 0.25° or 1° . In this sense, PARADIS maintains higher spectral coherence than the baseline models, reflecting better phase alignment and reduced structural drift.

F.4. Cyclone Tracking and Intensity

This appendix provides implementation details for the tropical cyclone track and intensity evaluation reported in Section 4.4 and summarized in Figure 7. Our objective is to enable a scale-aware, model-agnostic comparison while avoiding selection artifacts and ensuring consistent storm coverage across models.

To assess tropical cyclone forecast quality, we compare predicted storm tracks and intensities against the International Best Track Archive for Climate Stewardship (IBTrACS), treating IBTrACS (Gahtan et al., 2024) as ground truth. We perform a seasonal aggregation over the 2020 evaluation year and restrict the analysis to storms for which all evaluated models provide complete forecast coverage, yielding 84 storms and ensuring a like-for-like comparison. Each model is evaluated at its native spatial resolution.

For each model forecast time, the predicted cyclone center is identified as the minimum mean sea-level pressure (MSLP; denoted msl) within a geographic search window centered on the last known storm position, seeded from IBTrACS. All great-circle distances are computed using the Haversine formula.

IBTrACS provides storm positions and intensities at regular synoptic intervals. Model forecasts are verified at the same valid times. When model output timestamps do not exactly coincide with IBTrACS times, we select the closest model valid time within a tolerance window (e.g., ± 3 hours); forecasts without a match within this tolerance are excluded for that verification time.

For each storm and verification time, we compute the Direct Position Error (DPE) as the great-circle distance between the

predicted center and the IBTrACS reference position:

$$\text{DPE}(t) = d_{\text{gc}} \left((\phi_t^{\text{pred}}, \lambda_t^{\text{pred}}), (\phi_t^{\text{ref}}, \lambda_t^{\text{ref}}) \right), \quad (43)$$

where $d_{\text{gc}}(\cdot, \cdot)$ denotes the Haversine distance.

Intensity error is computed as the absolute error in minimum central pressure:

$$\text{IE}(t) = \left| msl_{\text{min}}^{\text{pred}}(t) - p_{\text{WMO}}^{\text{ref}}(t) \right|, \quad (44)$$

where $msl_{\text{min}}^{\text{pred}}(t)$ is the predicted minimum MSLP at the identified center and $p_{\text{WMO}}^{\text{ref}}(t)$ is the WMO-reported central pressure from IBTrACS. Intensity error is aggregated using mean absolute error across storms and verification times at each lead time.

Figure 7(a) shows the evolution of position error with lead time. PARADIS produces track forecasts that are at least as accurate as those of the machine-learning baselines and consistently more accurate than those of the physics-based HRES model.

At the same time, the 1° grid of PARADIS cannot fully resolve the inner cores of tropical cyclones. As a result, the model exhibits systematically higher central pressures (Figure 7(b)), corresponding to weaker resolved storms. This bias is dominated by errors in the gridded initial conditions and leads to a weakening trend similar to that observed in other machine-learning models, with convergence at lead times beyond approximately two days. PARADIS-AMSE mitigates this systematic weakening, consistent with the spectral-loss effects reported by Subich et al. (2025).

F.5. Skill at Higher Resolution

While the matched-resolution comparison isolates the quality of the learned operators, it does not directly reflect performance when baselines are evaluated at their native 0.25° resolution. To address this, we additionally compare relative skill against HRES on the original 0.25° grid. Since PARADIS produces forecasts at 1° , its outputs are interpolated to 0.25° prior to scoring using the same verification framework.

Figure 16 reports relative skill with respect to HRES for each model under this protocol. Despite its coarser native resolution, PARADIS remains competitive at longer lead times, where forecast errors are increasingly dominated by large-scale transport and phase errors rather than fine-scale detail. This behavior is expected given the architectural emphasis on coherent long-range dynamics, and it demonstrates that the improvements observed at matched resolution are not an artifact of regridding the baseline models. Instead, they reflect enhanced long-range transport behavior that persists even when evaluated under higher-resolution scoring.

G. Ablation Studies

To evaluate the relative importance of the components within the model, we conduct a series of ablation experiments. By systematically disabling the advection, diffusion, and reaction operators, we quantify their individual contributions to the overall predictive skill.

The parameter counts for each ablation configuration are summarized in Table 8.

Table 8. Model complexity across ablation configurations. C denotes the latent dimension, H the hidden dimension, and K the rank of the global bias.

Configuration (1deg)	Parameter count	Inference time
Full PARADIS	37M	3.3451s
No Advection	28M	2.0051s
No Diffusion	28M	2.4747s
No Reaction	19M	2.6431s

Our ablation experiments confirm that physically inspired semi-Lagrangian advection significantly benefits latent-space weather forecasting, as reflected in the model's performance. The *no advection* configuration was the worst-performing model by a significant margin, despite retaining the full capacity of the reaction and diffusion operators at a cost of 5M

parameters (14% of the full-model total). Its impact on the z_{500} geopotential error is more severe than removing the 18M parameter reaction block. This provides compelling evidence that the NSL advection is a powerful nonlinearity that allows the network to maintain physical consistency over time. It is known that advection is notoriously difficult for standard networks to learn without a dedicated geometric operator. In many cases, the use of attention mechanisms is a substitute for this operation, but their adherence to physical structure remains low.

H. NSL Operator versus U-Net

The gold standard for transporting information long distances with a convolutional backbone is the U-Net, which combines local convolutions, channel deepening, and spatial coarsening via pooling. In principle, this combination allows the model to transport or diffuse rich information (with many latent channels) over long distances in the deeper layers, while the shallower and more local topmost layers perform refinement. Residual connections help ensure training stability. This structure is illustrated for the U-Net of depth 3 in Figure 19.

This convolutional architecture, however, fixes a domain of dependency in its structure, and attempts to transport information beyond this domain will fail catastrophically. In contrast, the NSL layer has no such fixed, architectural limit, and its performance is more likely to degrade gracefully on harder transport problems.

To demonstrate this, we conduct a simple overfitting test to measure the overall capacity of these architectures. On a domain consisting of a latitude/longitude grid at quarter-degree resolution, a single-channel tracer field distributed as a Gaussian is placed at an arbitrary location on the sphere, and it is advected along a great circle arc towards the northeast over various angles a_i . The learning objective is to find the parameters θ_i that minimize $\int (\text{model}(\text{input}; \theta_i) - \text{target}_i)^2 dA$, or the area-weighted mean square difference between the prediction and target. Note that one model is trained per advection angle, giving the models maximum opportunity to overfit.

Table 9. Hyperparameters and total number of trainable parameters for the models of Figure 21 and Section H.

Model Name	Depth	Top layer channels	Total parameters
NSL	— N/A —	20	
UNet1	1	16	39,473
UNet2	2	8	44,617
UNet3	3	4	45,909

U-Net models of recursive depths 1 through 3 form the baseline, and they are configured with hyperparameters given in Table 9. The deeper U-Nets have fewer channels at their top layer in order to approximately equilibrate the number of parameters, and the residual difference is due to the up and down-projections found in the first encoder and last encoder layer to transform to and from the single-channel physical space. The deeper U-Nets have a larger receptive field, but the shallower U-Nets have a denser channel structure that can transport richer information.

In contrast, the Neural semi-Lagrangian model consists of a single 3×3 convolution with one input and two output channels. When combined with bias terms, these outputs define the local advection velocities used for gridded interpolation.

The final training losses over a selection of advection angles are shown in Figure 20. As the advection angle increases, each of the U-Nets successively “hits a wall” beyond which it is unable to effectively learn the correct flow. In contrast, the performance of the NSL model degrades more slowly and gracefully, with its chief limit being the distortion caused by the curvature of the grid. Model error fields are illustrated in Figure 21

I. Learned Operators and Latent Fields

To assess the internal representations learned by PARADIS, we take a look at the structure of some learned operators and resulting latent feature maps. By visualizing components of the hidden state, we can qualitatively verify that the model’s physically inspired inductive biases translate into physically structured, geographically coherent corrections and transport patterns.

Reconstructed bias maps. A key component for the Reaction and Diffusion blocks is the low-rank bias module. Figure 22 displays a representative subset of the reconstructed bias maps B' within the model. Many of these maps exhibit clear,

large-scale spatial structures that correlate with geographic features or zonal atmospheric patterns, suggesting that the network is learning systematic, geographically-structured corrections. However, it is important to note that this structured behavior is not universal across all channels. Some bias maps exhibit significant noise or unstructured patterns, which likely represent high-frequency stochastic corrections or unconstrained degrees of freedom within the latent representation.

Qualitative relationship between physical and latent winds. The NSL layer relies on an internally estimated velocity field \mathbf{u}_l to perform transport in latent space. In Figure 23, we compare the vertically averaged physical wind speeds with the averaged latent wind speed estimates by the NSL layers across different forecast lead times. The latent velocity fields exhibit a clear qualitative relationship with the physical wind atmospheric flows. As the forecast lead time increases, both the physical and latent fields develop greater spatial complexity, yet the model maintains a consistent transport topology, while showing some smoothed-out behavior.

J. Methods

J.1. Spherical Geometry

The implementation of the semi-Lagrangian scheme in spherical coordinates is inspired by (McDonald & Bates, 1989), who introduced an “auxiliary spherical coordinate system” to address difficulties near the poles. For each arrival point (ϕ_a, λ_a) , a rotated coordinate system (ϕ', λ') is defined, where the origin coincides with the arrival point, and the equator of this rotated system passes through the point in question. In this local system, λ' measures the angular distance along the rotated equator, while ϕ' measures the angular distance perpendicular to it.

When applying the geocyclic padding described in Section 3.2.4, there is a difficulty in handling wind vectors near the Earth’s poles due to the convergence of meridians, which creates artificial discontinuities in the latitude-longitude coordinate system. This would force the neural networks to learn unnatural, discontinuous transformations in their latent space representations. Hence, we propose to transform wind vectors from spherical coordinates into Cartesian coordinates in a pre-processing step. This transformation avoids the coordinate singularity at the poles and ensures a locally continuous representation of winds. The transformation from spherical velocity components (u, v, w) to Cartesian components (u_x, u_y, u_z) is given by

$$\begin{aligned} u_x &= -u \sin(\lambda) - v \sin(\phi) \cos(\lambda) - w \cos(\phi) \cos(\lambda), \\ u_y &= u \cos(\lambda) - v \sin(\phi) \sin(\lambda) - w \cos(\phi) \sin(\lambda), \\ u_z &= v \cos(\phi) - w \sin(\phi). \end{aligned}$$

Then, the neural network operates on these continuous Cartesian components, and the output is transformed back to spherical coordinates during post-processing. The inverse transformation is given by

$$\begin{aligned} u &= -u_x \sin(\lambda) + u_y \cos(\lambda), \\ v &= -u_x \sin(\phi) \cos(\lambda) - u_y \sin(\phi) \sin(\lambda) + u_z \cos(\phi), \\ w &= -u_x \cos(\phi) \cos(\lambda) - u_y \cos(\phi) \sin(\lambda) - u_z \sin(\phi). \end{aligned}$$

J.2. Radiation Parameterization

Following the approach of (Lam et al., 2023), we include the one-hour accumulated top-of-atmosphere (TOA) incoming solar radiation as an external conditioning channel for the forecast model. This variable provides the network with an implicit representation of the time of day and seasonality. Because the model is not provided with sufficient information to compute a full radiative balance, this signal serves primarily as a temporal and geometric proxy rather than a physically complete radiation scheme.

The computation closely follows (Wald, 2019), accounting for the ellipticity of Earth’s orbit while neglecting variability in the solar cycle. Let ϕ denote latitude, λ longitude, and T the Julian day referenced to 1 January 2000 at 12:00 UTC. The instantaneous TOA incoming solar radiation, R is given by

$$\begin{aligned} R(\phi, \lambda, T) &= \frac{1360.56}{d(T)^2} \max \left(0, \sin(\phi) \sin(\delta(T)) \right. \\ &\quad \left. + \cos(\phi) \cos(\delta(T)) \cos(t(T, \lambda)) \right). \end{aligned} \tag{45}$$

The orbital and solar geometry parameters required to evaluate (45)—including the Earth–Sun distance $d(T)$ and solar declination $\delta(T)$ —are summarized in Table 10. All angular quantities are reduced to the interval $[-\pi, \pi]$ during computation.

The local solar time $t(T, \lambda)$ depends on the equation of time $\text{EOT}(T) = L(T) - \alpha(T)$, and is computed as:

$$t(T, \lambda) = \lambda + 2\pi T + \text{EOT}(T). \quad (46)$$

The final conditioning variable provided to the model corresponds to the one-hour accumulated TOA radiation, obtained by integrating (45) over the one-hour interval ending at the specified time.

Table 10. Orbital and solar geometry parameters used for radiation evaluation.

Parameter	Equation
Obliquity	$\epsilon(T) = \frac{\pi}{180}(23.439 - 3.6 \times 10^{-7}T)$
Mean Anomaly	$M(T) = \frac{\pi}{180}(357.529 + 0.985600028T)$
Mean Longitude	$L(T) = \frac{\pi}{180}(280.459 + 0.98564736T)$
Sun Longitude	$\lambda_{\odot}(T) = L(T) + \frac{\pi}{180}(1.915 \sin M + 0.020 \sin 2M)$
Earth–Sun Dist.	$d(T) = 1.00014 - 0.01671 \cos M - 1.4 \times 10^{-4} \cos 2M$
Right Ascension	$\alpha(T) = \arctan(\cos \epsilon \tan \lambda_{\odot})$
Declination	$\delta(T) = \arcsin(\sin \epsilon \sin \lambda_{\odot})$

K. Visual Forecast Examples

Finally, we present qualitative results for the PARADIS and PARADIS-AMSE models compared to the ERA5 reference analysis. Each figure shows the evolution of a specific meteorological field at 6-hour, 5-day, and 10-day lead times. For each time step, the subplots represent (left) the ERA5 reference, (middle) the PARADIS forecast, and (right) the PARADIS-AMSE forecast.

L. Table of Symbols

The following table summarizes the primary symbols and notations used to describe the PARADIS architecture and its underlying physical principles.

Symbol	Description / Definition
State Variables and Domains	
\mathbf{q}	Physical state vector of atmospheric variables.
\mathbf{h}	Latent state vector/features.
\mathbf{x}	Grid point location.
\mathbf{x}_d	Departure point at time t found by tracing trajectories backward.
\mathbf{u}	Velocity field or transport velocities satisfying $d\mathbf{x}/dt = \mathbf{u}$.
ϕ	Latitude.
λ	Longitude.
Model Operators	
$\mathcal{A}_{\text{net}}, \mathcal{A}$	Neural Semi-Lagrangian (NSL) operator for advection.
$\mathcal{D}_{\text{net}}, \mathcal{D}$	Neural operator for diffusion-like spatial mixing.
$\mathcal{R}_{\text{net}}, \mathcal{R}$	Neural operator for local reaction/source terms.
\mathcal{V}_{net}	Velocity network estimating transport fields from the latent state.
\mathcal{I}	Bicubic interpolation.
N_{sub}	Number of processor layers/substeps to advance from t to $t + \Delta t$.
\mathcal{E}	Encoder mapping physical variables to latent space.
\mathcal{G}	Decoder mapping latent space back to physical space.
$\frac{D}{Dt}$	Material derivative ($\frac{\partial}{\partial t} + \mathbf{u} \cdot \nabla$).
Model Architecture	
K	Rank for low-rank factorization of the global bias field.
H, W	Dimension of spatial grid.
\mathbf{W}	Weight matrix.
\mathbf{K}_d	A channel-wise spatial filter applied independently on each channel.
\mathbf{b}	Learned bias.
$\mathbf{A}, \mathbf{U}, \mathbf{V}$	Factor matrices for low-rank bias decomposition.
\mathbf{B}	Low-rank bias map.
\mathbf{z}	Projected state in latent space projection.
Optimization and Training	
L_δ	Reversed Huber loss function.
\tilde{L}_δ	Pseudo-reversed Huber loss function.
δ	Threshold parameter for the Huber loss transition.
e	Prediction error.
w	A sigmoid weighting function.
β_1, β_2	AdamW optimizer momentum hyperparameters.
Meteorological variables	
z	Geopotential
t	Temperature
u	u -component of wind (zonal)
v	v -component of wind (meridional)
w	vertical velocity
q	Specific humidity
$2t$	2-metre temperature
$10u$	10-metre u -component of wind
msl	Mean sea-level pressure

Table 11. Summary of mathematical notation in the PARADIS architecture.

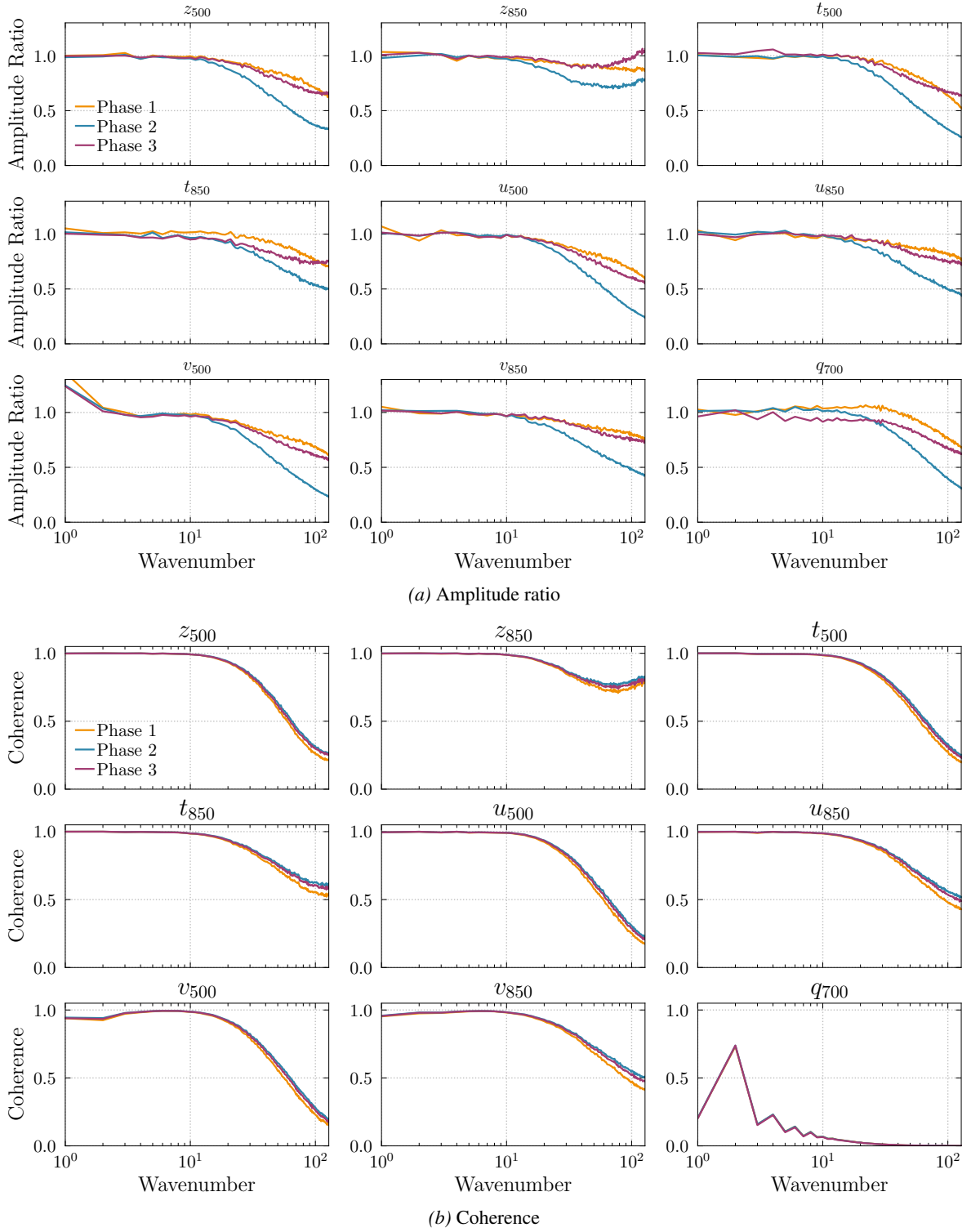


Figure 10. Amplitude ratios ((a), closer to 1 is better) and coherence ((b), higher is better) plots for PARADIS after training phases 1, 2, and 3 for several variables at 72h lead time

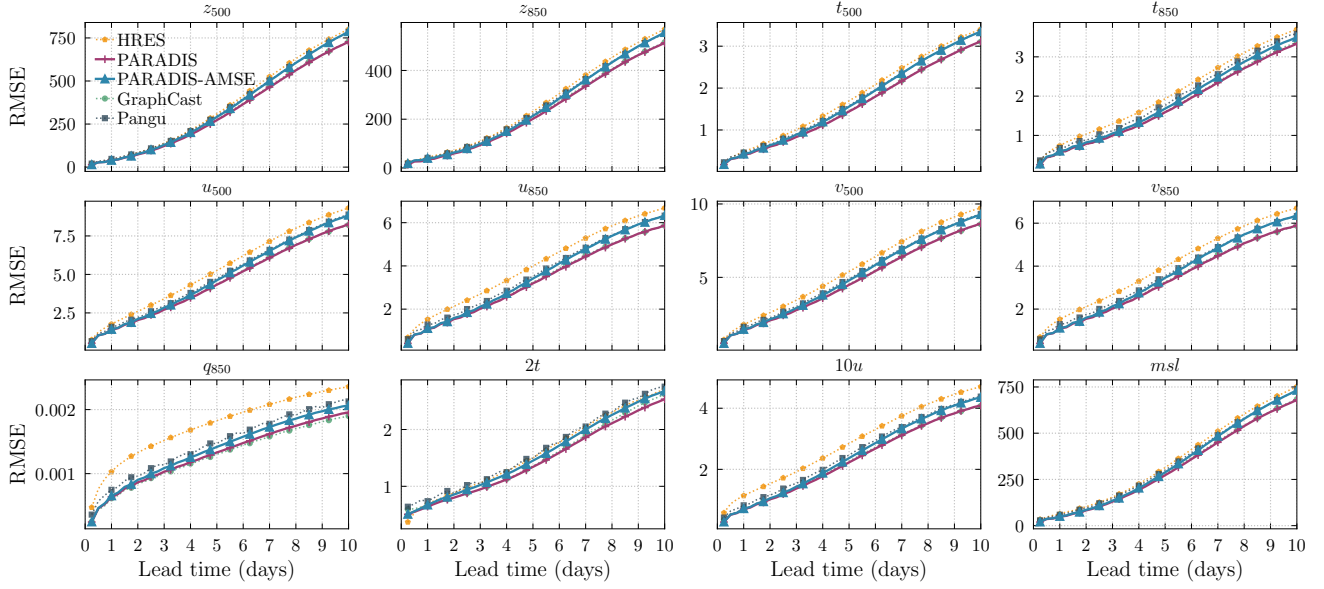


Figure 11. Comparison of forecast performance between PARADIS, PARADIS-AMSE, GraphCast, Pangu, and HRES as a function of lead time. Each panel displays the Root Mean Square Error (RMSE, lower is better) for key atmospheric variables. PARADIS demonstrates consistent improvements in error across variables.

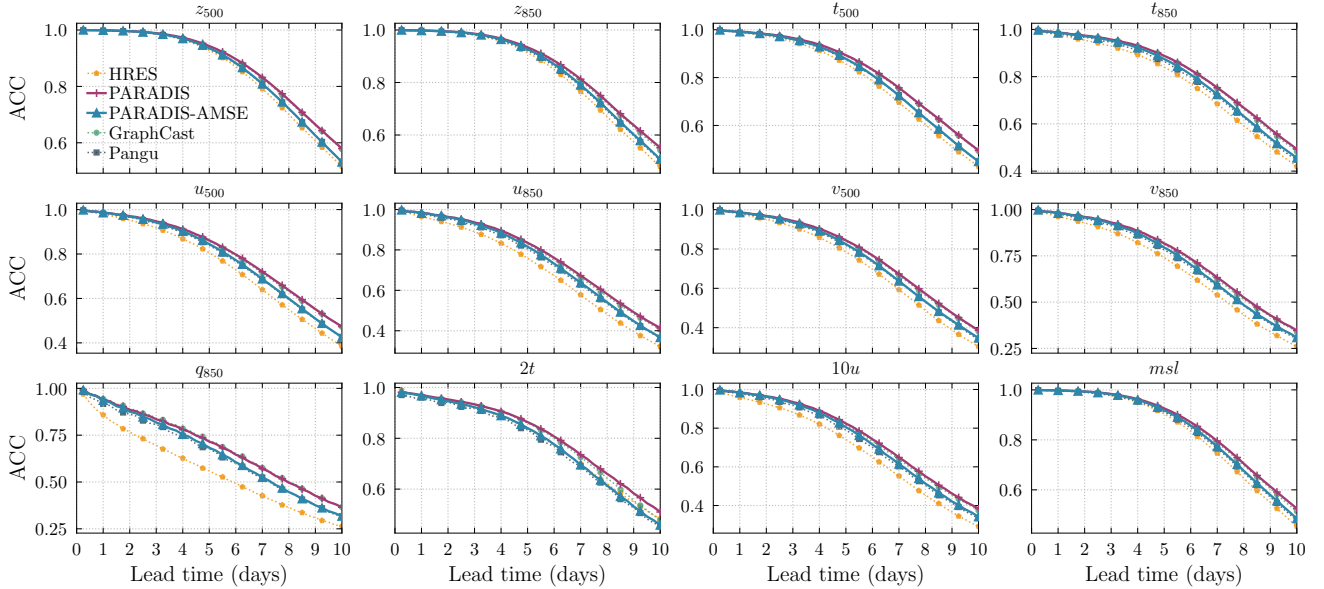


Figure 12. Comparison of anomaly correlation coefficient (ACC, higher is better) between PARADIS, PARADIS-AMSE, GraphCast, Pangu, and HRES as a function of lead time, evaluated at matched 1° resolution. Each panel shows ACC for a key atmospheric variable. PARADIS maintains higher correlation at longer lead times, indicating improved phase accuracy and large-scale pattern retention.

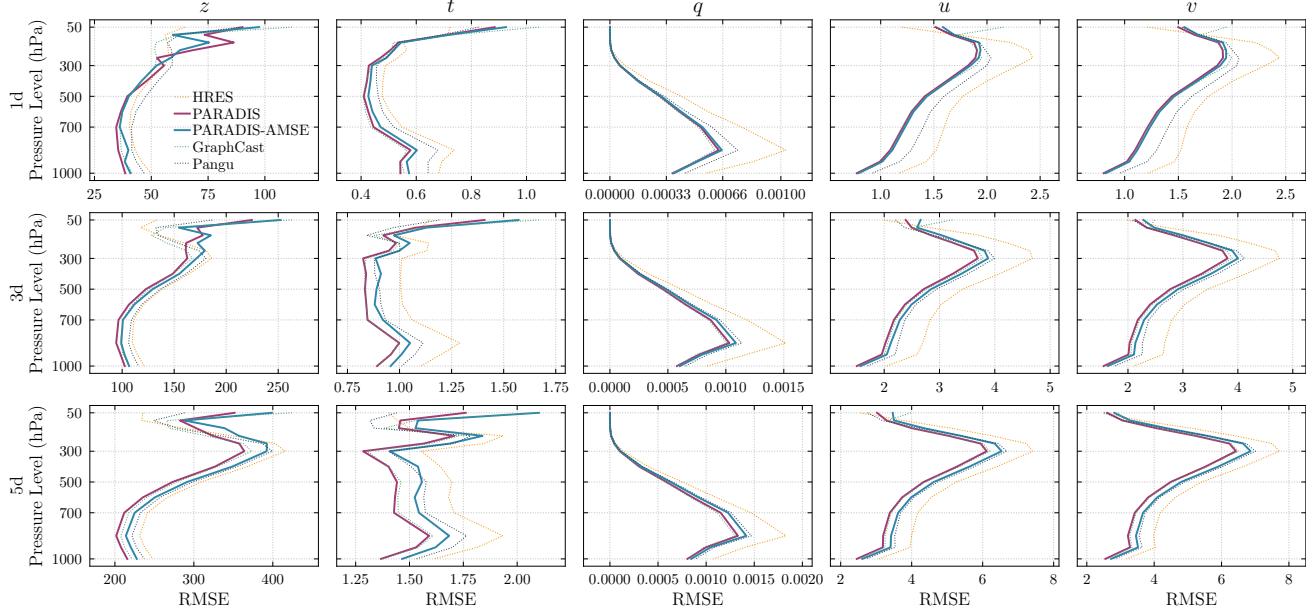


Figure 13. Vertical distribution of error for the PARADIS model as a function of pressure level across all lead times.

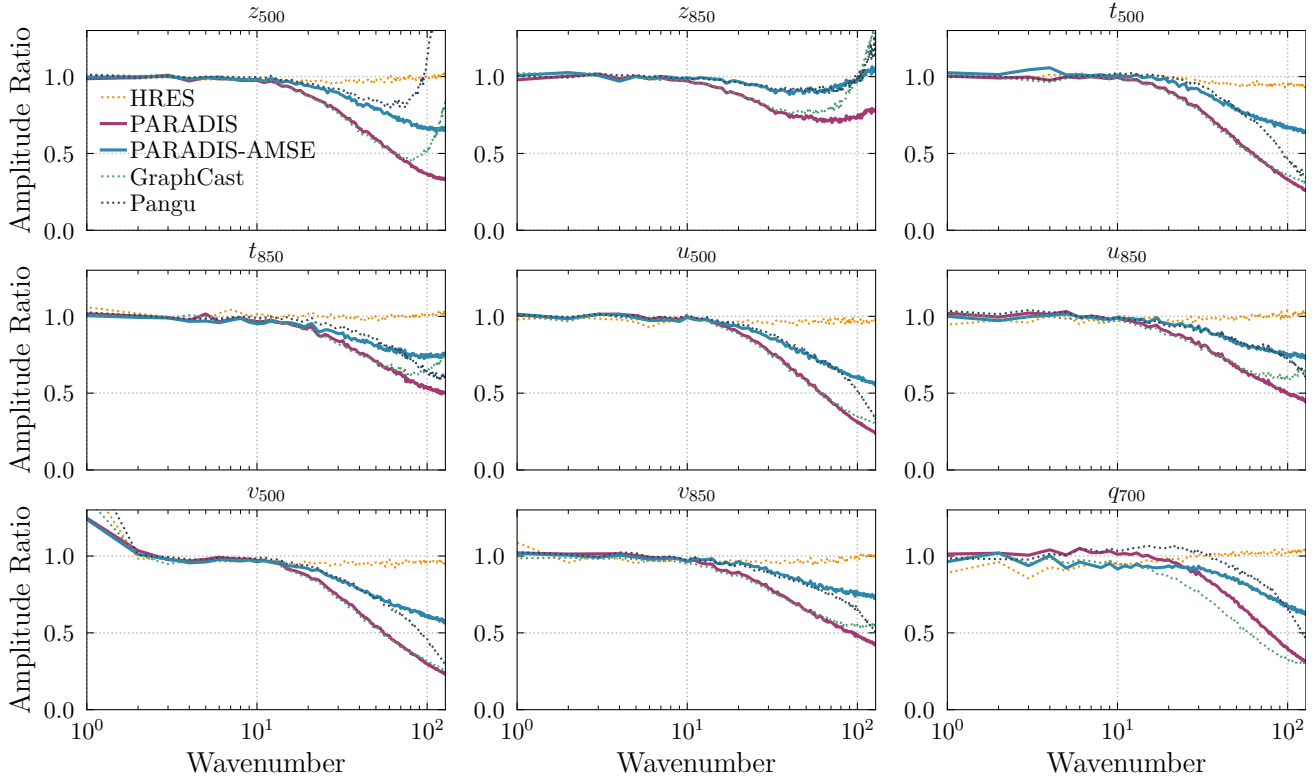


Figure 14. Comparison of spectral performance between PARADIS, PARADIS-AMSE, GraphCast, Pangu, and HRES at 72h lead time. Each panel displays the amplitude ratio (closer to 1 is better) for key atmospheric variables.

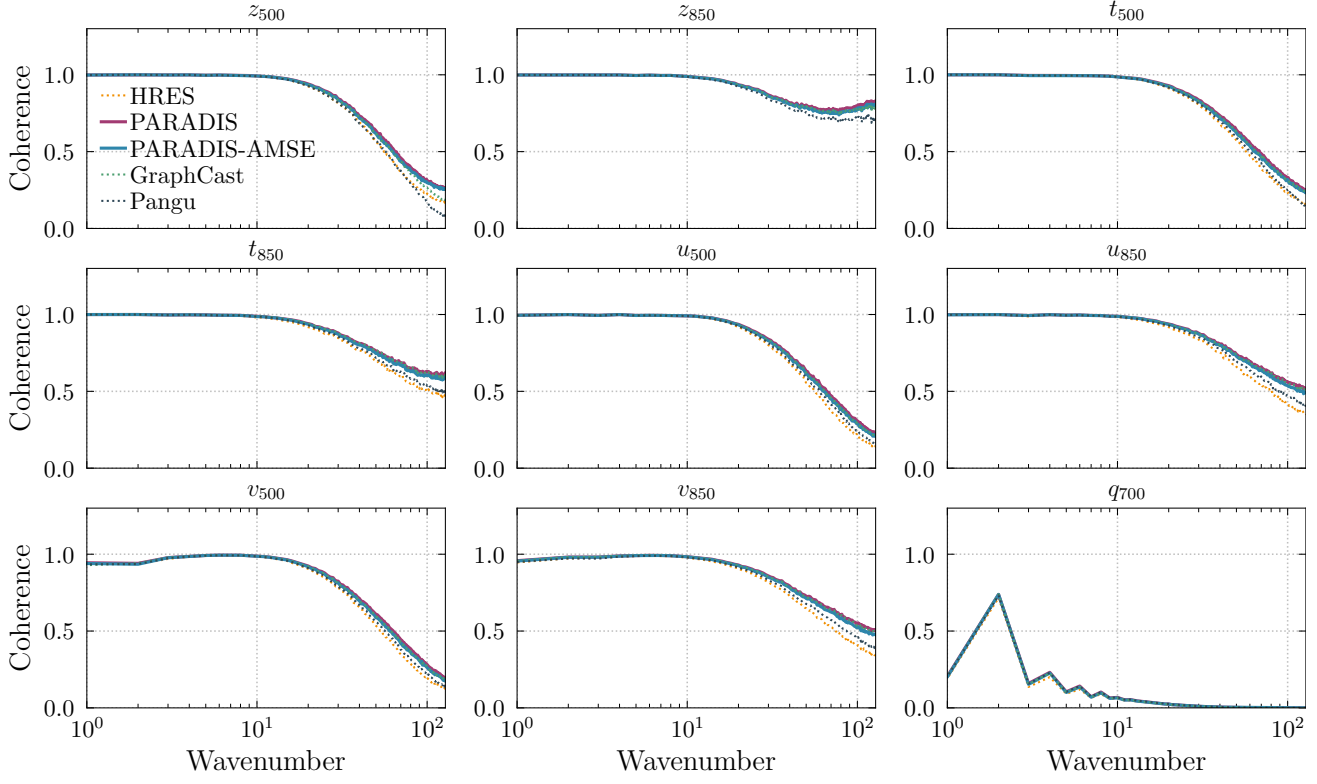


Figure 15. Comparison of spectral performance between PARADIS, PARADIS-AMSE, GraphCast, Pangu, and HRES at 72h lead time. Each panel displays the coherence for key atmospheric variables.

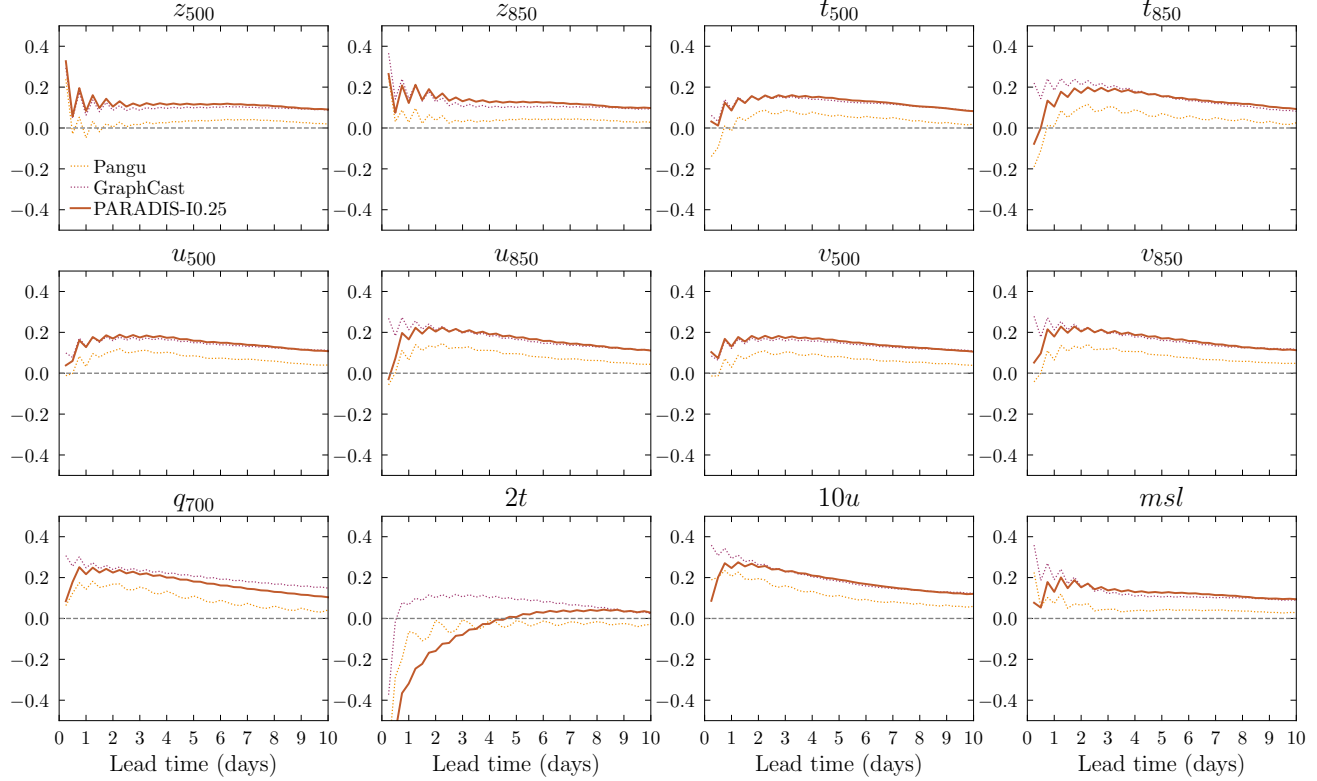


Figure 16. Relative skill (higher is better) against HRES of different models at their original 0.25-degree grid, including PARADIS interpolated to this resolution.

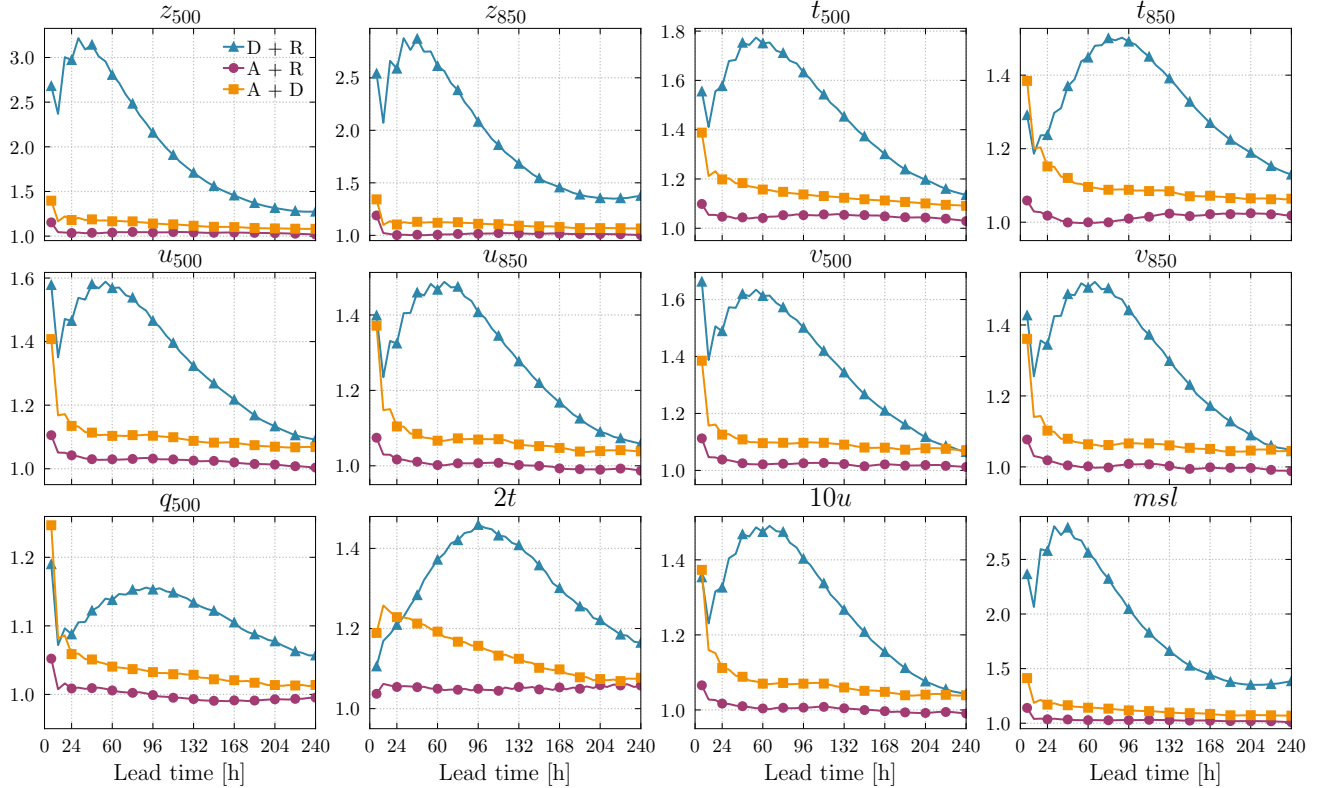


Figure 17. Normalized RMSE (lower is better) versus lead time for different ablation experiments across variables and vertical levels. Errors are shown relative to the baseline model. The impact of removing individual physical components varies by variable and lead time, with the largest degradation generally observed when advection is omitted.

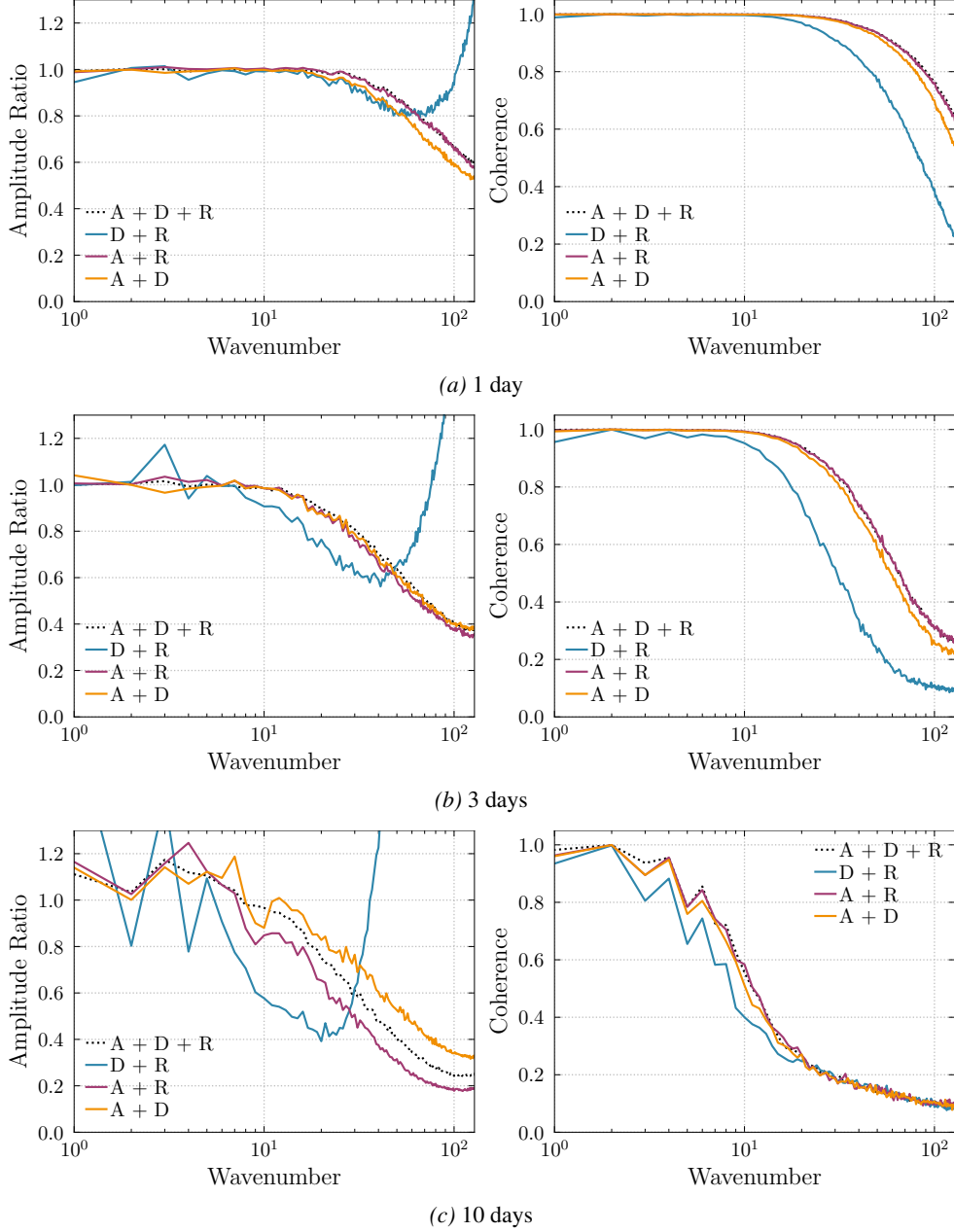


Figure 18. Amplitude ratio (left column; closer to 1 is better) and spectral coherence (right column; higher is better) of z_{500} as functions of total spherical wavenumber for the full PARADIS model (A+D+R) and ablated variants without advection (D+R), diffusion (A+R), or reaction (A+D). Rows correspond to forecast lead times of (a) 1 day, (b) 3 days, and (c) 10 days. The removal of advection leads to a rapid loss of amplitude and coherence at intermediate and small scales, while models retaining advection preserve spectral energy and phase alignment substantially longer. This highlights advection as the dominant mechanism for maintaining multiscale structure over extended lead times.

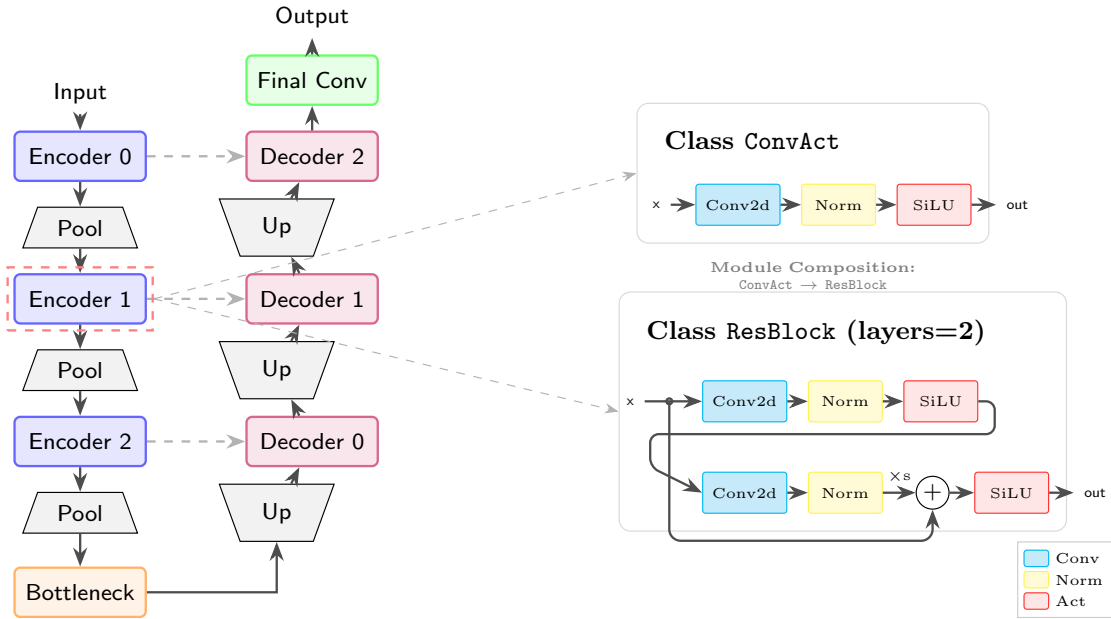


Figure 19. Structural diagram of the U-Net of depth 3.

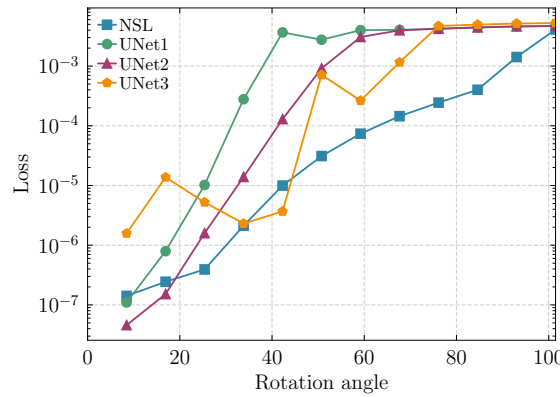


Figure 20. Final training loss of the Gaussian advection test case, by advection angle

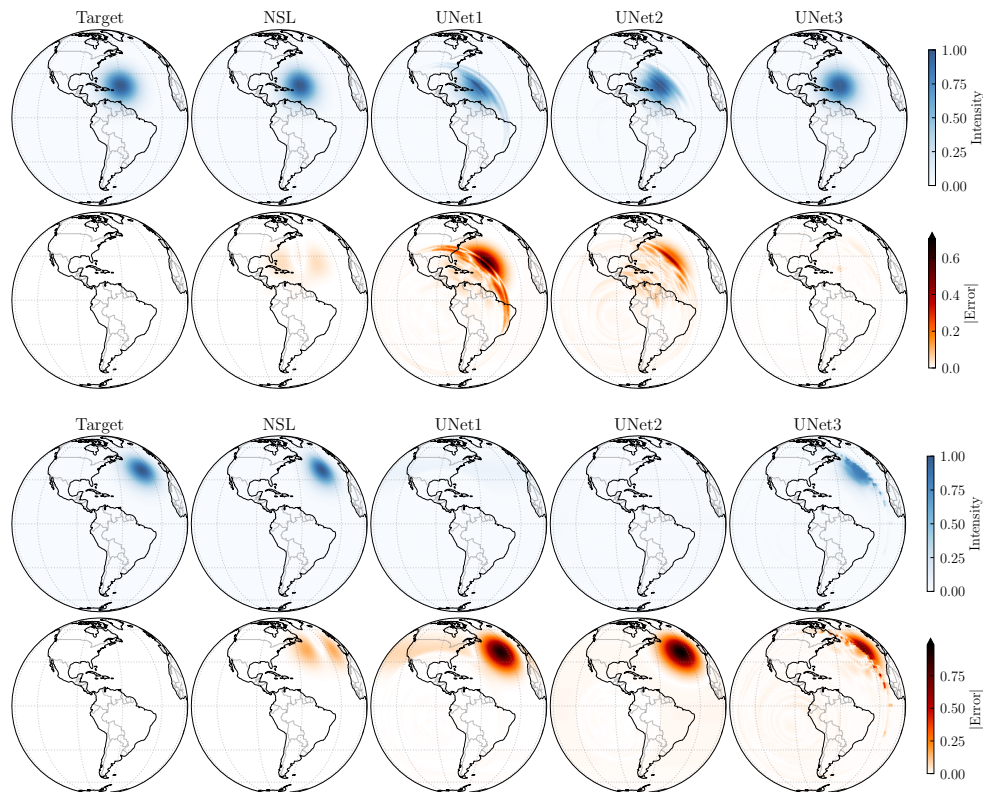


Figure 21. Rows 1 and 2: Model outputs and errors, respectively, for a 42° rotation, inside the domain of dependence for the U-Net of depth 3, but not depth 1 or 2. Rows 3 and 4: Outputs and errors, respectively, for a 68° rotation, where the deeper U-Net struggles.

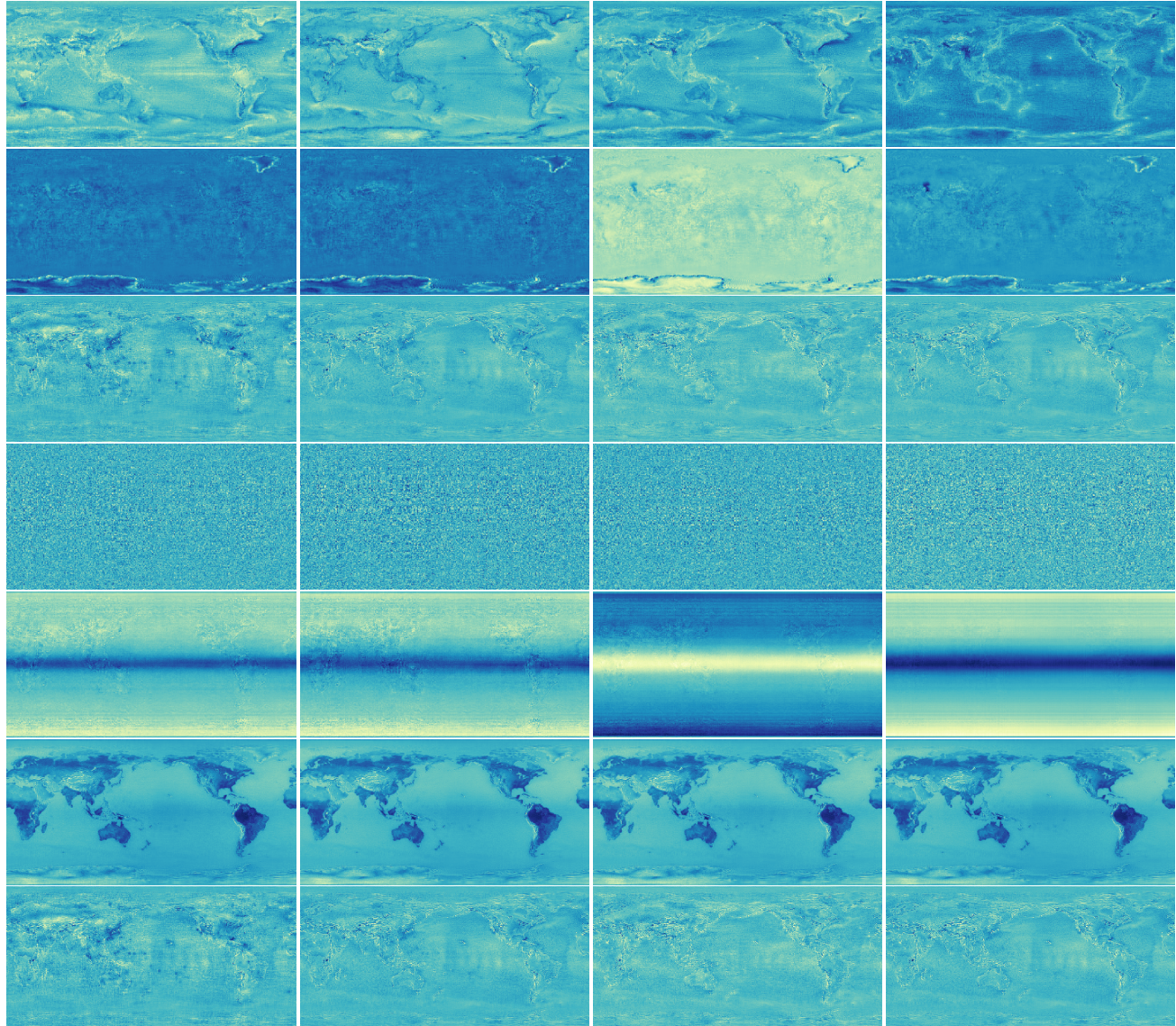


Figure 22. Representative examples of reconstructed low-rank bias maps. Each panel shows a selected channel of the intermediate bias tensor B' reconstructed from the learned rank- K factors (A, U, V) in the low-rank bias module (Section B.1.3). For clarity, only a subset of channels is shown. The bias maps exhibit spatially coherent structure, suggesting that the model learns large-scale, geographically structured corrections in latent space.

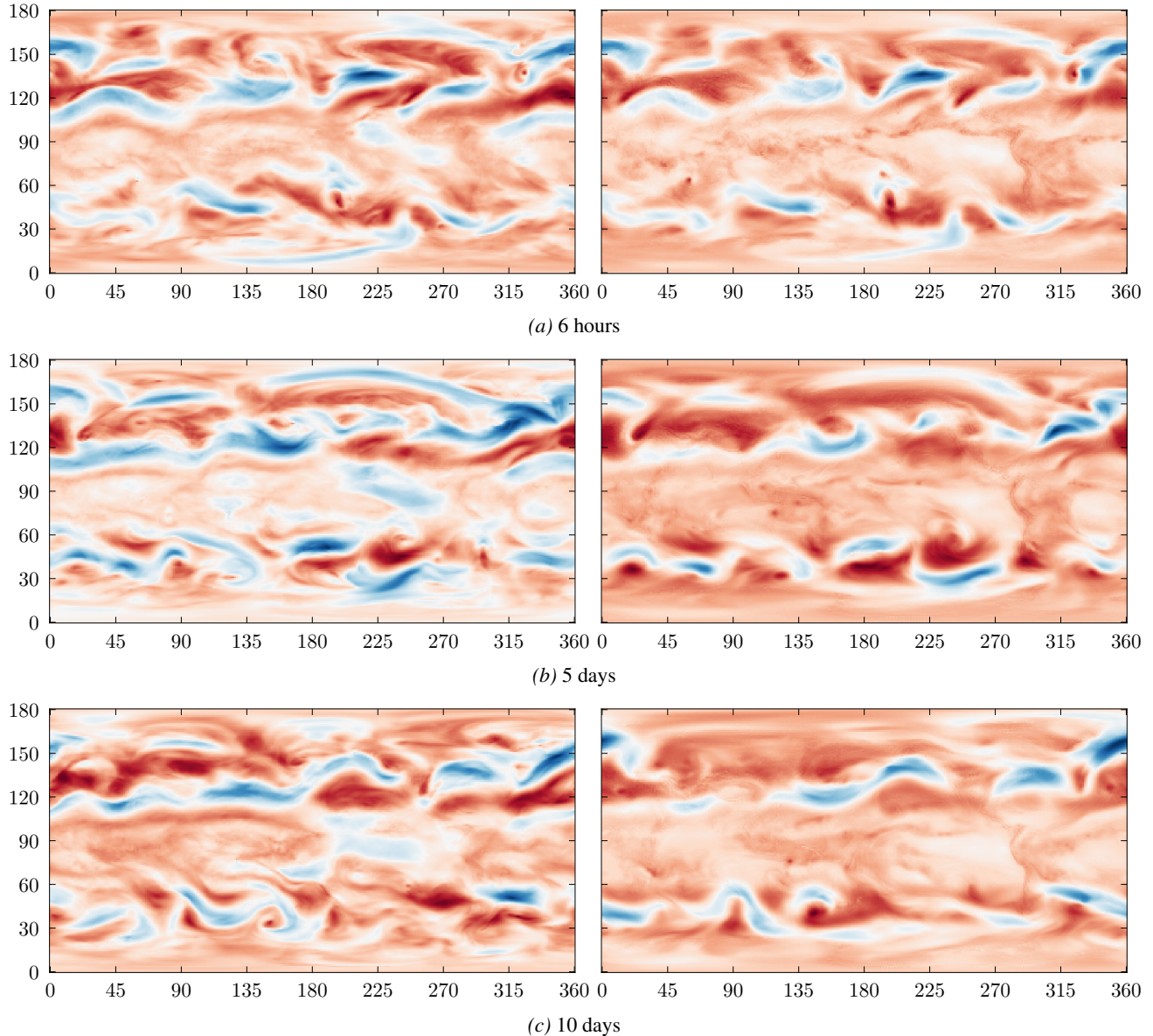


Figure 23. Evolution of sample learned velocity fields across forecast lead times. **Left** panels show vertically averaged physical wind speed, while **right** panels display the corresponding averaged latent wind speed, aggregated over all channels and layers of the Neural Semi-Lagrangian advection module. Results are shown for (a) 6 hours, (b) 5 days, and (c) 10 days lead time. The fields exhibit coherent, large-scale flow structures and increasing spatial complexity with lead time, indicating that the model learns physically consistent transport patterns in latent space.

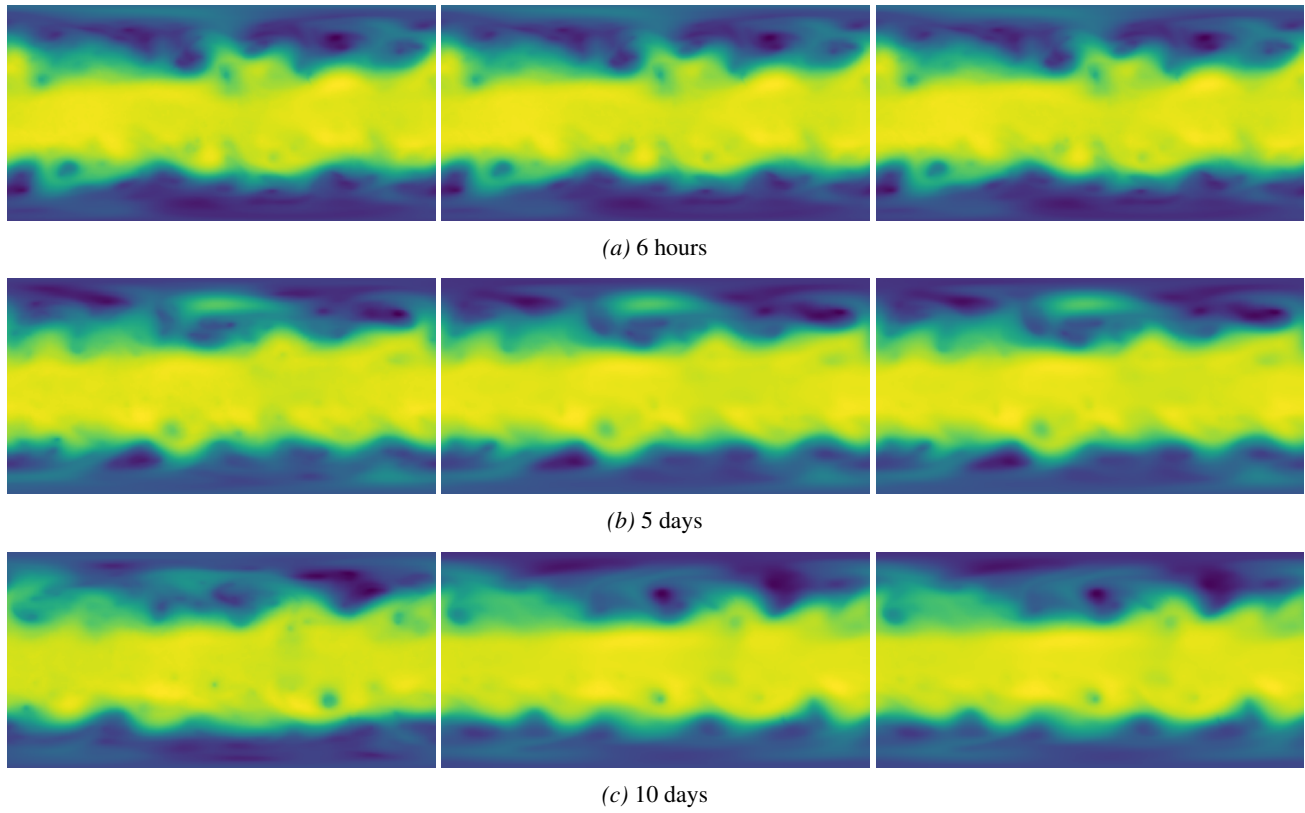


Figure 24. Field: Geopotential at 500 hPa. Left plot is the reference, middle plot is PARADIS, right plot is PARADIS-AMSE

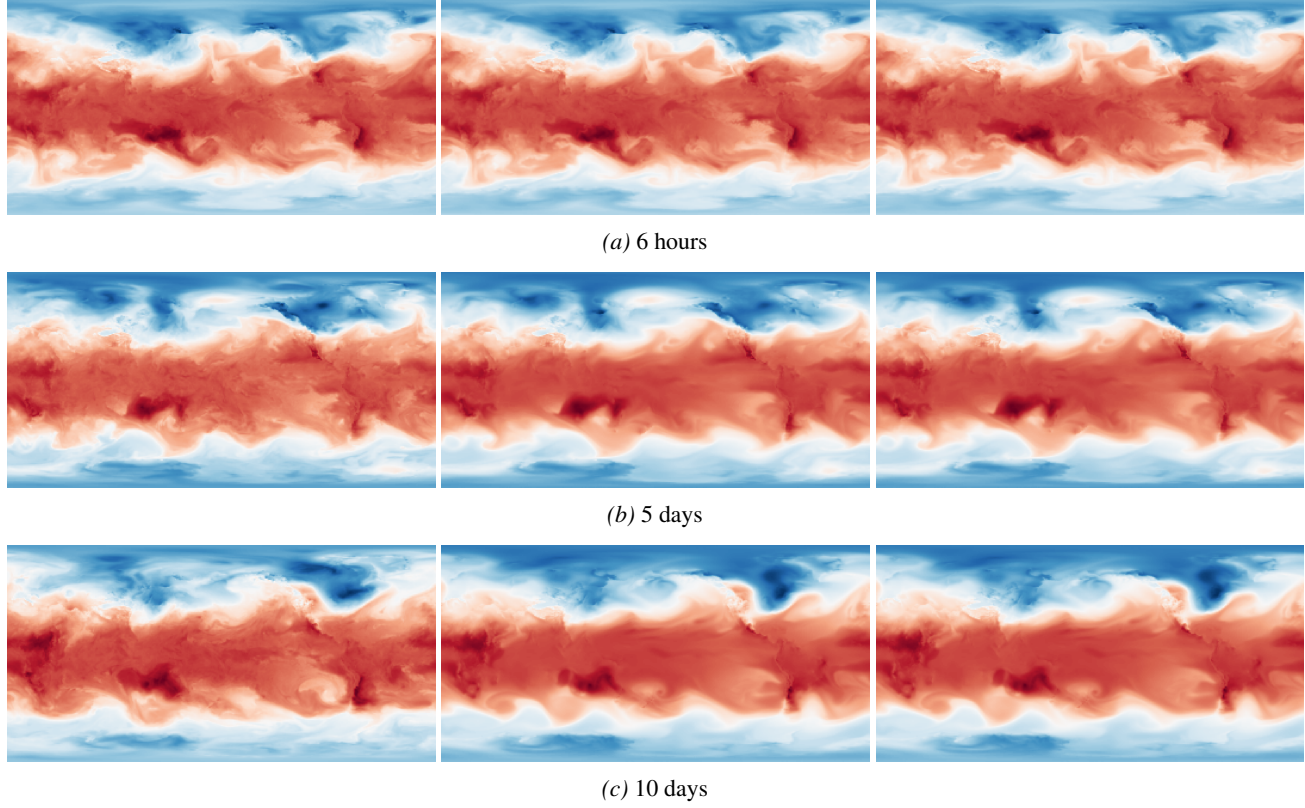


Figure 25. Field: Temperature at 850 hPa. Left plot is the reference, middle plot is PARADIS, right plot is PARADIS-AMSE

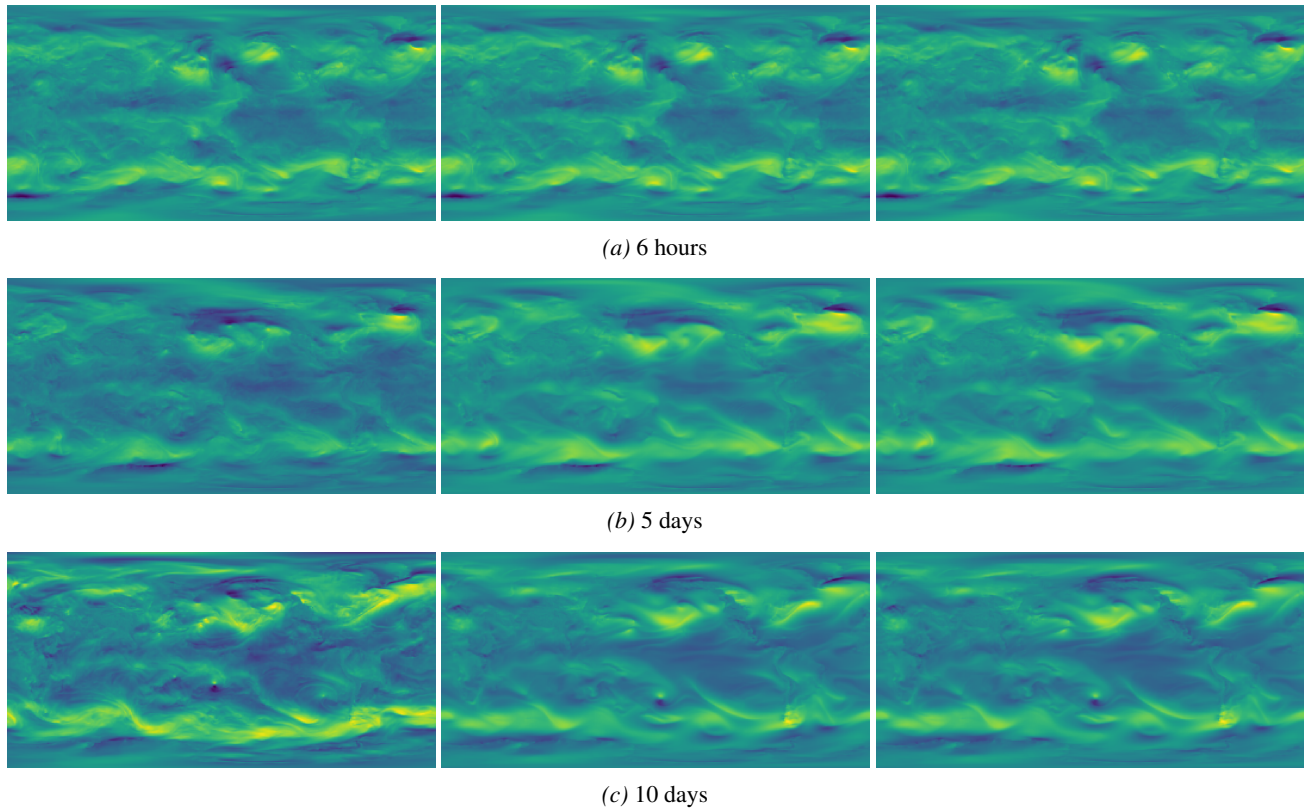


Figure 26. Field: u -component of wind at 850 hPa. Left plot is the reference, middle plot is PARADIS, right plot is PARADIS-AMSE

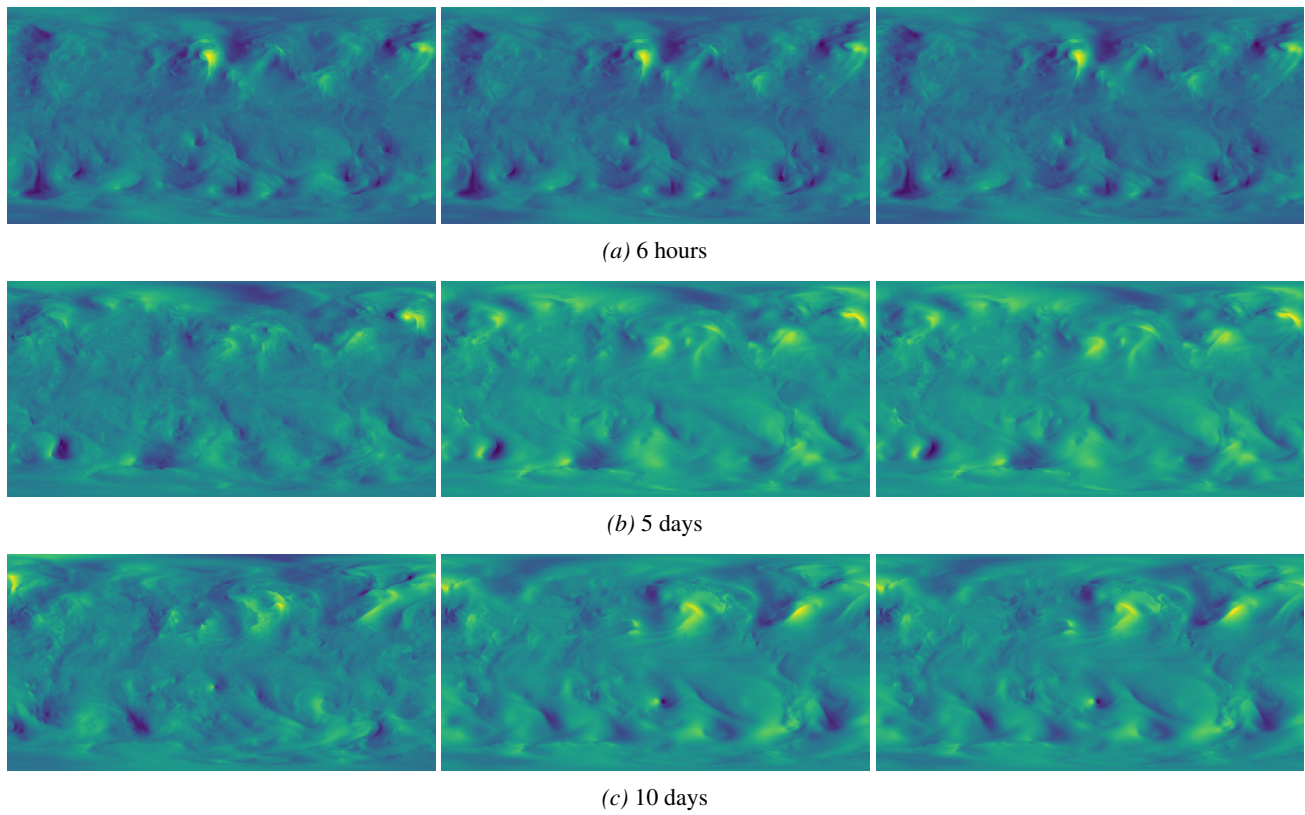


Figure 27. Field: v -component of wind at 850 hPa. Left plot is the reference, middle plot is PARADIS, right plot is PARADIS-AMSE

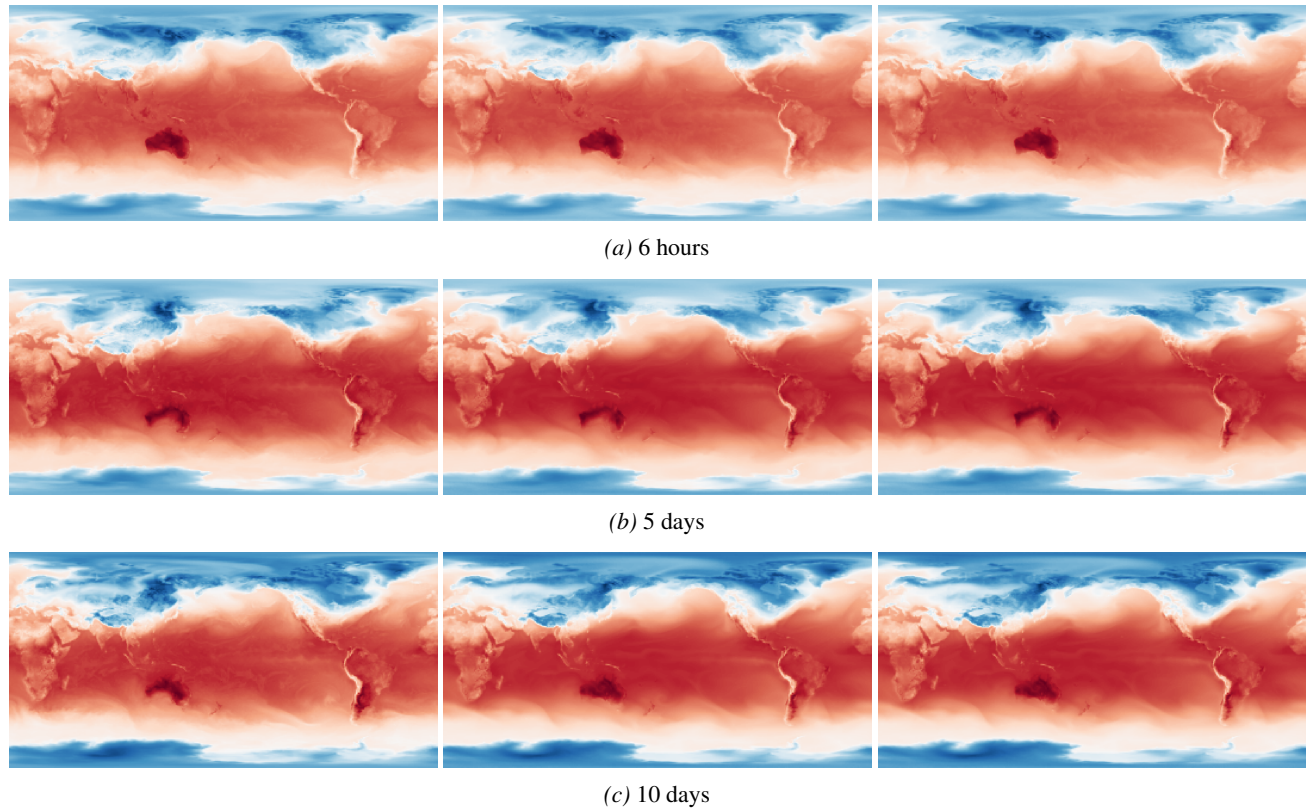


Figure 28. Field: 2m-temperature. Left plot is the reference, middle plot is PARADIS, right plot is PARADIS-AMSE